Biophysical Journal
Article

Biophysical Society

Neutron scattering maps the higher-order assembly of NADPH-dependent assimilatory sulfite reductase

Daniel T. Murray,[1] Nidhi Walia,[1] Kevin L. Weiss,[2] Christopher B. Stanley,[2,3] Peter S. Randolph,[1] Gergely Nagy,[2] and M. Elizabeth Stroupe[1,*]

[1]Department of Biological Science and Institute of Molecular Biophysics, Florida State University, Tallahassee, Florida; [2]Neutron Scattering Division, Oak Ridge National Laboratory, Oak Ridge, Tennessee; and [3]Computational Sciences and Engineering Division, Oak Ridge National Laboratory, Oak Ridge, Tennessee

ABSTRACT Precursor molecules for biomass incorporation must be imported into cells and made available to the molecular machines that build the cell. Sulfur-containing macromolecules require that sulfur be in its S^{2-} oxidation state before assimilation into amino acids, cofactors, and vitamins that are essential to organisms throughout the biosphere. In α-proteobacteria, NADPH-dependent assimilatory sulfite reductase (SiR) performs the final six-electron reduction of sulfur. SiR is a dodecameric oxidoreductase composed of an octameric flavoprotein reductase (SiRFP) and four hemoprotein metalloenzyme oxidases (SiRHPs). SiR performs the electron transfer reduction reaction to produce sulfide from sulfite through coordinated domain movements and subunit interactions without release of partially reduced intermediates. Efforts to understand the electron transfer mechanism responsible for SiR's efficiency are confounded by structural heterogeneity arising from intrinsically disordered regions throughout its complex, including the flexible linker joining SiRFP's flavin-binding domains. As a result, high-resolution structures of SiR dodecamer and its subcomplexes are unknown, leaving a gap in the fundamental understanding of how SiR performs this uniquely large-volume electron transfer reaction. Here, we use deuterium labeling, in vitro reconstitution, analytical ultracentrifugation (AUC), small-angle neutron scattering (SANS), and neutron contrast variation (NCV) to observe the relative subunit positions within SiR's higher-order assembly. AUC and SANS reveal SiR to be a flexible dodecamer and confirm the mismatched SiRFP and SiRHP subunit stoichiometry. NCV shows that the complex is asymmetric, with SiRHP on the periphery of the complex and the centers of mass between SiRFP and SiRHP components over 100 Å apart. SiRFP undergoes compaction upon assembly into SiR's dodecamer and SiRHP adopts multiple positions in the complex. The resulting map of SiR's higher-order structure supports a *cis*/*trans* mechanism for electron transfer between domains of reductase subunits as well as between tightly bound or transiently interacting reductase and oxidase subunits.

SIGNIFICANCE NADPH-dependent assimilatory sulfite reductase (SiR) is an essential metabolic enzyme that performs reduction of environmental sulfur for biomass formation. SiR is a two-component oxidoreductase with an unusual, asymmetric stoichiometry composed of an octameric reductase flavoprotein (SiRFP) and four independent oxidase hemoproteins (SiRHPs). Although we know the structures of the individual subunits as monomers, we do not know how they assemble into the dodecameric holoenzyme. Conventional studies by X-ray crystallography and cryoelectron microscopy are frustrated by SiR's large size and inherent flexibility. Presented here, small-angle neutron scattering has allowed us to visualize the relative positioning of the two subunits and show that the SiRHP subunits are independent of one another at the periphery of the complex, tethered by SiRFP.

INTRODUCTION

Multicomponent enzyme complexes play pivotal roles in metabolic, electron transport, and signaling pathways where quaternary protein complexes assemble to allow intra- and inter-subunit domain-domain interactions enabling catalysis (1–4). In these complexes, subunits containing individual catalytic domains oligomerize into macromolecular machines that integrate enzymatic functions into cohesive processes. Multicomponent enzymes are potentially beneficial because they can channel pathway intermediates to control metabolic flux, allow for higher efficiency, and prevent harmful intermediate release from active sites (4). In the case of multicomponent oxidoreductases, combining

Submitted November 18, 2021, and accepted for publication April 15, 2022.

*Correspondence: mestroupe@bio.fsu.edu

Editor: John J. Correia.

https://doi.org/10.1016/j.bpj.2022.04.021

oxidase and reductase subunits into a unified machinery enables them to perform high-volume electron transfer reactions. Isolated oxidase or reductase subunits are often well characterized structurally; however, their assemblies can be challenging to characterize because the domains within individual subunits can be connected by flexible linkers that change conformation based on assembly state (5,6). NADPH-dependent assimilatory sulfite reductase (SiR) is one such oxidoreductase (7).

SiR catalyzes the electron transfer reduction-oxidation (redox) reaction prerequisite to sulfur's incorporation into biomolecules. Specifically, sulfite (SO_3^{2-}) undergoes a six-electron reduction to sulfide (S^{2-}) through the coordinated action of SiR's flavoprotein (α, or SiRFP) subunits and hemoprotein (β, or SiRHP) subunits (Fig. 1 *A*) (8). SiR holoenzyme is a 792-kDa $\alpha_8\beta_4$ hetero-dodecamer composed of 67-kDa diflavin reductases that assemble into a 536-kDa flavoprotein octamer with four 64-kDa hemoprotein metalloenzymes that we will refer to as a dodecamer for simplicity (Fig. 1 *B*) (9). Each SiRHP subunit binds one of four separate SiRFP subunits (9,10). The mismatched

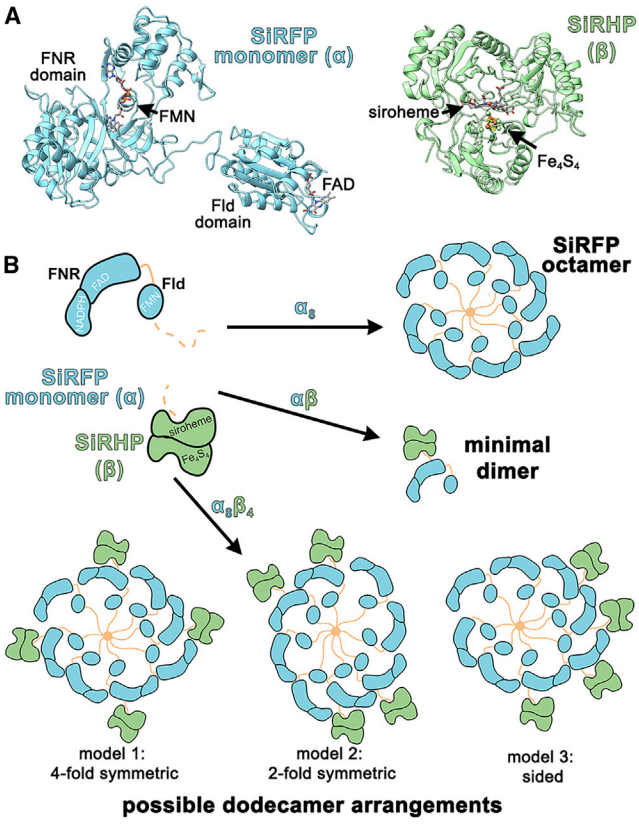

FIGURE 1 SiR is a modular oxidoreductase. (*A*) X-ray crystal structures of SiRFP (*blue*, PDB: 6EFV) and SiRHP (*green*, PDB: 1AOP) subunits. (*B*) Full-length SiRFP spontaneously forms a homo-octamer, whereas SiRHP is a monomer. N-terminally truncated SiRFP is also a monomer that can bind a single copy of SiRHP to form a minimal heterodimer. Octameric SiRFP binds four independent SiRHPs in an unknown arrangement. Various subunit arrangements are possible to account for SiR's $\alpha_8\beta_4$ stoichiometry.

stoichiometry between reductase and oxidase subunits differentiates SiR from similar oxidoreductases and is thought to contribute to the efficiency of its high-volume electron transfer reaction (3,11–13).

SiRFP shares similar flavin adenine dinucleotide (FAD)- and flavin mononucleotide (FMN)-binding domains with other diflavin reductases, whose FAD- and FMN-binding domains are homologous to ferredoxin-$NADP^+$ reductase (FNR) domains and flavodoxins (Flds), respectively (Fig. 1 *A*) (14). SiRFP channels electrons from NADPH through FAD and FMN cofactors before transferring them to the siroheme and Fe_4S_4 cluster cofactors of the SiRHP subunits (Fig. 1 *A*) (15). This electron transfer sequence is enabled by the nanomolar affinity between SiRFP and SiRHP subunits, with SiRHP binding to SiRFP's FNR domain through its N-terminal 80 amino acids (16,17).

SiRFP is hypothesized to transfer electrons between its cofactors by a redox-sensitive domain motion enabled by the flexible linker of 30 residues in length between its FNR and Fld domains, similar to its well-characterized homolog cytochrome P450 reductase (CPR) (18,19). In oxidized CPR, the Fld domain is in a closed conformation relative to the FNR domain, such that, when NADPH reduces the FNR-bound FAD, it is in close proximity to the Fld-bound FMN (20–22). Upon subsequent FAD reduction and NAD^+ release, the Fld domain extends to create the transient cytochrome P450 binding site for electron transfer (23,24). Electron transfer by SiRFP could behave in an analogous fashion; however, unlike CPR, oxidized SiRFP monomer adopts an extended conformation between its domains (7,14). Additionally, SiRFP's Fld domain further extends upon binding its SiRHP oxidase, whereas the CPR-cytochrome *c* dimer is compact (5), with cytochrome *c* binding in a cleft between the Fld and FNR domains (5,7).

SiR's subunits are modular, which allows them to be examined as simplified monomers (i.e., isolated α or β components) or a 1:1 heterodimer (αβ), by expressing the α subunit as an N-terminal truncation, the β subunit on its own, or a mixture of the two, respectively (Fig. 1 *B*) (25–27). The SiR heterodimer is active for SO_3^{2-} reduction but with reduced efficiency compared with the dodecamer (25,28). Truncating SiRFP's flexible linker further diminishes activity in the heterodimer but, importantly, not as significantly in the dodecamer (14). This observation suggests a model in which electron transfer occurs through both intramolecular and intermolecular pathways in the complex. For example, electrons might pass from an NADPH to the FAD of SiRFP before either passing to the FMN bound to the same polypeptide, or to an FMN bound to another SiRFP within the dodecamer. Additionally, electrons may also pass between SiRFP and an SiRHP that is directly bound to its FNR domain, or to a SiRHP that is its neighbor in the complex. This model is supported by solution scattering of the SiR heterodimer, which shows that SiRFP possesses sufficient conformational malleability to allow its Fld

domain to move into the vicinity of neighboring subunits (7). Further, anaerobically reduced SiRFP projects its Fld domain toward the binding interface with SiRHP (7). Such a *cis/trans* mechanism for electron transfer within SiR is in analogy to nitric oxide synthase, whose reductase domain is a SiRFP homolog, where the reductase domain of one subunit approaches the oxidase domain of another in a domain-swapping manner (3,29). Redundant electron donor/acceptor pairing, enabled by its stoichiometry and flexibility, may help explain how SiR performs its high-volume electron transfer without releasing partially reduced intermediates (30–33).

Ultimately, the lack of structural information for dodecameric SiR leaves unanswered questions regarding how the subunits position relative to one another, what interactions support those positions, and how domain motions regulate electron transfer (Fig. 1 *B*). Here, we use a combination of deuterium labeling, in vitro reconstitution, analytical ultracentrifugation (AUC), small-angle neutron scattering (SANS), and neutron contrast variation (NCV) to discern the nature and effects of higher-order assembly by SiR. The ability to reconstitute native-like complexes from individually purified subunits allows assembly between partially deuterated SiRHP (D-SiRHP) and hydrogenated SiRFP to form D-SiR. Molecular weights (MWs) and sedimentation coefficients (Svedberg units [S]) determined by SANS and AUC, respectively, support SiR's hypothesized $\alpha_8\beta_4$ stoichiometry. SiR's solution-state structure exhibited both globularity and conformational malleability as a result of its large, multicomponent structure containing flexible linkers in each of its eight SiRFP subunits. Subsequently, an NCV series measured on D-SiR isolated the scattering contributions of each subunit. Structural insights obtained through NCV reveal the asymmetric organization of SiR, including centers of mass and separation of each component, with SiRHP subunits adopting multiple positions at the periphery of the complex, tethered by a central SiRFP octamer that compacts upon dodecamer assembly. Collectively, these studies provide an initial mapping of SiR's higher-order structure with implications for its mode of electron transfer.

MATERIALS AND METHODS

SiR expression, purification, and reconstitution

Hydrogenated SiR proteins were expressed and purified as previously described (14,16,17). In summary, pBAD vectors (Thermo Fisher Scientific, Waltham, MA, USA) containing genes encoding hexa-histidine tagged, full-length *Escherichia coli* SiRFP octamer (*cysJ*), N-terminally truncated monomer (SiRFP-60), or a tricistronic hexa-histidine tagged SiRFP/SiRHP (*cysI*)/siroheme synthase (*cysG*) construct (SiR dodecamer) were individually transformed into *E. coli* LMG194 cells (Invitrogen, Carlsbad, CA, USA) and induced with 0.5% L-arabinose for expression in Luria Bertani broth at 25°C. SiRFP, SiRFP-60, or SiR were purified to homogeneity through a combination of nickel affinity, anion exchange, and size-exclusion chromatography (SEC). Hydrogenated and partially deuterated SiRHP (D-SiRHP) were also expressed and purified as previously described (7). Briefly, a pBAD vector encoding bicistronic *cysI* and *cysG* was transformed into *E. coli* BL21 (DE3) cells (New England Biolabs, Ipswich, MA, USA) and protein was expressed in Enfors minimal media containing either H_2O (hydrogenated SiRHP) or 70% D_2O (D-SiRHP), induced with 0.05% L-arabinose at 25°C (34). SiRHP and D-SiRHP were purified through a series of ammonium sulfate precipitation, desalting, anion exchange, and SEC steps.

Purified SiRFP was mixed with 6 molar equivalents (Eq) D-SiRHP and incubated for 2 h on ice to form the D-SiR dodecamer. SiRFP-60/D-SiRHP heterodimer was assembled by mixing SiRFP-60 with 2 Eq D-SiRHP followed by an identical incubation. Excess D-SiRHP was used during reconstitution to saturate the binding capacity of SiRFP variants and maximize complex recovery upon chromatographic separation of free subunits. Reconstituted complexes were then loaded onto a 5-mL HisTrap FF nickel affinity chromatography column (Cytiva, Marlborough, MA, USA) that had been equilibrated with 50 mM KPi, pH 7.8, 100 mM NaCl, and eluted with a gradient of the same buffer containing 500 mM imidazole. Fractions containing the assembled complexes were loaded onto a Superose 6 10/300 SEC column (Cytiva, Marlborough, MA, USA) equilibrated with SANS buffer (50 mM KPi, pH 7.8, 100 mM NaCl, 1 mM EDTA) to isolate the specimen of interest. Final preparations were analyzed with SDS-PAGE and compared to -visible (UV-vis) absorption to ensure its purity and correct stoichiometry.

Sedimentation velocity AUC

Sedimentation velocity experiments were performed using a ProteomeLab XL-1 analytical ultracentrifuge equipped with an AN60-Ti rotor and Epon two-channel centerpieces (Beckman Coulter, Brea, CA, USA). SiR samples were adjusted with SANS buffer to 0.3 mg/mL, yielding an absorbance of approximately 0.5 at 280 nm as measured with an 8454 UV-vis spectrophotometer (Agilent Technologies, Santa Clara, CA, USA). Samples were loaded into cell assemblies with sapphire windows appropriate for absorbance data. Rotor speeds of 40,000 or 25,000 rpm were used for monomeric D-SiRHP or higher-order SiR samples, respectively. All samples were run at 20°C for 7 h. Scan data were imported into UltraScan III software, where they were edited and underwent 2D spectrum analyses (2D-SA) to obtain MW (AUC MW) values and frictional ratios (f/f_0) (35,36). In the same software, sedimentation coefficient envelopes were obtained through enhanced van Holde-Weischet analyses. S values were corrected for the density and viscosity of SANS buffer at 20°C ($S_{20,w}$).

SANS measurements

Hydrogenated SiR proteins were dialyzed into SANS buffer prepared with 100% D_2O prior to SANS measurements, whereas partially deuterated complexes were dialyzed into buffers with various H_2O:D_2O ratios to perform an NCV series of measurements. The contrast match points (CMPs) of the complex's components were determined as previously described (7). In brief, the CMP of hydrogenated SiRFP (41% D_2O) was determined from theoretical calculations of its scattering length density based on protein sequence, isotopic content, and solvent conditions (37). Alternatively, the CMP of D-SiRHP (86% D_2O) was determined experimentally by performing an NCV series of SANS measurements (7,38–40). Knowing each component's CMP, D-SiR was dialyzed into SANS buffer containing 0%, 20%, 41%, 86%, or 100% D_2O. SiRFP-60/D-SiRHP was dialyzed into 0%, 41%, 86%, or 100% D_2O. The concentration of each protein sample was quantified post dialysis using a NanoDrop One UV-vis spectrophotometer (Thermo Fisher Scientific, Waltham, MA, USA) prior to loading into cuvettes (Table S1).

SANS data were collected on the extended Q-range small-angle neutron scattering diffractometer (EQ-SANS, Beam Line 6) at the Spallation Neutron Source (SNS), Oak Ridge National Laboratory (ORNL) (41). Samples were loaded into 1-mm pathlength circular quartz cuvettes (Hellma

USA, Plainville, NY, USA) and data collected at 8°C with the simultaneous introduction of dry air to prevent condensation on the exterior of the cuvettes. Three instrument configurations were used in 60-Hz operation mode to obtain the relevant wavevector transfer, $Q = 4\pi\sin(\theta)/\lambda$, where 2θ is the scattering angle and λ is the neutron wavelength: 9-m sample-to-detector distance with 15 Å wavelength band, 4-m sample-to-detector distance with 6 Å wavelength band, and 1.3-m sample-to-detector distance with 4 Å wavelength band (42). These configurations enabled acquisition of datasets with a Q range (0.002–0.72 $Å^{-1}$) that sufficiently captures the specimen's length scales. Scattering data were circularly averaged and reduced to one-dimensional scattering profiles using Mantid Workbench and Jupyter Notebooks (43,44). The measured scattering intensities were corrected for detector sensitivity and scattering contributions from buffers and empty cells, and then placed on an absolute scale using a calibrated Porasil B standard (45). Replicate measurements were summed and those from each instrument configuration were merged. Initial scattering data were compared with data from duplicate measurements at the end of each sample's data collection to ensure sample integrity. Incoherent background subtractions were also implemented in Mantid Workbench to correct for excess incoherent scattering from hydrogen in the sample before the datasets were exported for analysis.

SANS data analysis and modeling

Reduced, background-subtracted data were imported into BioXTAS RAW for analysis (46). Within this software, $P(r)$ calculations were performed using GNOM, which provided D_{max} values as previously described (7,14), as well as being used to provide R_g and $I(0)$ values (7,47,48). Similarly, Guinier analyses, dimensionless Kratky plots, and MW determinations from SANS (SANS MW) were generated in BioXTAS RAW (49–51).

The intensity of the SANS signal from biological macromolecules in solution depends on their contrast, which is the difference in scattering length density (SLD, or ρ) between the macromolecule and its solvent ($\Delta\rho = \rho_{\text{macromolecule}} - \rho_{\text{solvent}}$). Neutrons scatter from atomic nuclei, with differences arising from variations in atomic number and isotope. NCV series are made possible by the difference in scattering between hydrogen and deuterium, the abundance of the former in biomolecules, and the ability to substitute the latter in macromolecules and solvents. R_g values for a complex are related to contrast by Stuhrmann's equation, Eq. (1) (52):

$$R_g^2 = R_m^2 + \alpha\Big/\Delta\overline{\rho} - \beta\Big/\Delta\overline{\rho}^2, \tag{1}$$

where $\Delta\overline{\rho}$ is the mean contrast, R_m is the R_g of the complex at infinite contrast, and the coefficients α and β are associated with SLD (52,53). The α coefficient is related to the second moment of scattering density fluctuations about the mean for a scattering particle, whereas the β coefficient relates to the square of the first moment (54). The sign of α relates to a component's center of mass (COM) relative to that of the complex, and β is proportional to the square of the distance between each component's COM (D). α and β can be determined from Stuhrmann's equation by using a polynomial least-squares fit of R_g^2 against $\Delta\overline{\rho}^{-1}$. Throughout the current study, D-SiR's components are referred to in the context of their respective SLDs: hydrogenated SiRFP octamer as one component and four D-SiRHP subunits collectively comprising another component within D-SiR's two-component complex. SLD, $\Delta\overline{\rho}$, and the evaluation of the contrast dependence of R_g using Stuhrmann analyses were carried out in the Contrast and Rg modules of MULCh (37,52,55). SLD and $\Delta\overline{\rho}$ are calculated from protein sequence, isotopic content, and solvent condition inputs using the same software (37).

The parallel axis theorem (PAT), Eq. (2), can also be used to determine R_g and D values for a complex's components (54–56):

$$\begin{aligned} R_{\text{obs}}^2 = {} & \left((\Delta\overline{\rho}_1 V_1/\Delta\overline{\rho}V)R_1^2\right) + \left((\Delta\overline{\rho}_2 V_2/\Delta\overline{\rho}V)R_2^2\right) \\ & + \left((\Delta\overline{\rho}_1 V_1/\Delta\overline{\rho}V)(\Delta\overline{\rho}_2 V_2/\Delta\overline{\rho}V)D^2\right), \end{aligned} \tag{2}$$

where R_{obs} is the measured R_g, V is molecular volume, and R_1 and R_2 are the R_g of each component. The use of this approach was also performed using MULCh with the same input parameters used during Stuhrmann analysis (37).

GNOM $P(r)$ output files were used as inputs for ab initio modeling using DENSS or DENSS-Multiple to generate scattering envelopes, as previously described (7,57,58). Briefly, 20 reconstructions were generated in DENSS operating in "slow" mode, followed by their alignment, averaging, and refinement without the use of symmetry constraints. DENSS-Multiple of D-SiR was performed identically to DENSS modeling except with the use of $P(r)$ inputs from multiple SANS measurements: 0%, 20%, and 41% D_2O. Rigid body modeling of SiRHP's known monomeric structure against its scattering data was performed using SASREF (59). Where applicable, high-resolution structures obtained from the Protein Data Bank (PDB) were positioned into solution structures in UCSF ChimeraX (60,61). All SANS data (Table 1) and their associated models were deposited in the Small Angle Scattering Biological Data Bank (62) SASBDB: SASDMJ8 (SiR), SASDMK8 (SiRFP), SASDML8 (SiRHP), SASDMM8 (DSiR0), SASDMN8 (DSiR20), SASDMP8 (DSiR41), SASDMQ8 (DSiR86), SASDMR8 (DSiR100), SASDMS8 (SiRFP-60/D-SiRHP in 0% D_2O), SASDMT8 (SiRFP-60/D-SiRHP in 41% D_2O), SASDMU8 (SiRFP-60/D-SiRHP in 86% D_2O), and SASDMV8 (SiRFP-60/D-SiRHP in 100% D_2O).

DENSS models for D-SiRHP, SiRFP, and D-SiR were subsequently converted to bead models using EM2DAM, in All That Small Angle Scattering 3.0 (ATSAS 3.0) [63], and then theoretical R_g, MW, and S values for the models were calculated in UltraScan SOlution MOdeler (US-SOMO)

TABLE 1 SANS parameters for sulfite reductase

Protein	% D_2O	Oligomeric state	Domain or protein composition	R_g (Å)	D_{max} (Å)	MW (kDa)	SANS MW (kDa)[b]
SiR	100	dodecamer ($\alpha_8\beta_4$)	SiRFP/SiRHP	101.5 ± 0.9	325	802	830
D-SiR (DSiR0)	0	dodecamer ($\alpha_8\beta_4$)	SiRFP/D-SiRHP	105.0 ± 1.2	315	826	839
D-SiR (DSiR20)	20	dodecamer ($\alpha_8\beta_4$)	SiRFP/D-SiRHP	110.4 ± 3.2	315	826	
D-SiR (DSiR41)	41	dodecamer ($\alpha_8\beta_4$)	SiRFP[a]/D-SiRHP	96.7 ± 7.9	285	826	
D-SiR (DSiR86)	86	dodecamer ($\alpha_8\beta_4$)	SiRFP/D-SiRHP[a]	73.0 ± 0.7	220	826	
D-SiR (DSiR100)	100	dodecamer ($\alpha_8\beta_4$)	SiRFP/D-SiRHP	82.9 ± 0.8	245	826	
SiRFP-60/D-SiRHP	0	dimer ($\alpha\beta$)	Fld-linker-FNR/D-SiRHP	36.3 ± 0.7	130	128	136
SiRFP-60/D-SiRHP	41	dimer ($\alpha\beta$)	Fld-linker-FNR[a]/D-SiRHP	24.1 ± 0.6	66	128	
SiRFP-60/D-SiRHP	86	dimer ($\alpha\beta$)	Fld-linker-FNR/D-SiRHP[a]	33.1 ± 0.5	124	128	
SiRFP-60/D-SiRHP	100	dimer ($\alpha\beta$)	Fld-linker-FNR/D-SiRHP	41.3 ± 0.6	139	128	
SiRFP	100	octamer (α_8)	Octamerization-Fld-linker-FNR	80.8 ± 0.8	260	571	578
SiRHP	100	monomer (β)	SiRHP	23.3 ± 0.1	72	64	64.7

[a]The contrast-matched component.
[b]Only data at full contrast were used to obtain SANS MW.

(64). Theoretical conditions used as inputs in US-SOMO mirrored those of the AUC experiments (density, viscosity, pH, temperature).

RESULTS

SANS of dodecameric SiR

SiR's $\alpha_8\beta_4$ SANS profile exhibited separate plateaus at low and middle Q regions that arose from the higher-order complex and individual subunits, respectively, on length scales relative to the larger dodecamer and smaller monomeric components (Fig. 2 *A*). The R_g and D_{max} for the complex were 101.5 and 325 Å, respectively, whereas Guinier analysis indicated a monodisperse protein solution (Table 1 and Fig. S1 *A*). The $P(r)$ function of SiR had an interatomic vector length (r) peak around 128 Å and a shoulder at lower values of r that indicated distinct intra-subunit distances of differing scales within the complex (Figs. 2 *B* and S2 *A*). The gradual decay of the complex's $P(r)$ to its D_{max} indicated that SiR is extended in solution. Dimensionless Kratky analysis of SiR's scattering data demonstrates a Gaussian peak that then rises to a plateau, corresponding to a globular complex with a degree of flexibility (Fig. 2 *C*) (49,65). The absolute calibration of the SANS data was used to calculate the SANS MW of the SiR complexes (50,66), and the calculated SANS MW for the co-expressed SiR of 830 kDa was consistent with the theoretical MW of its his-tagged complex, 802 kDa (3.5% difference; Table 1). These analyses constitute the first solution-state characterization of SiR machinery to our knowledge, and provide an initial description of the extended, flexible dodecamer.

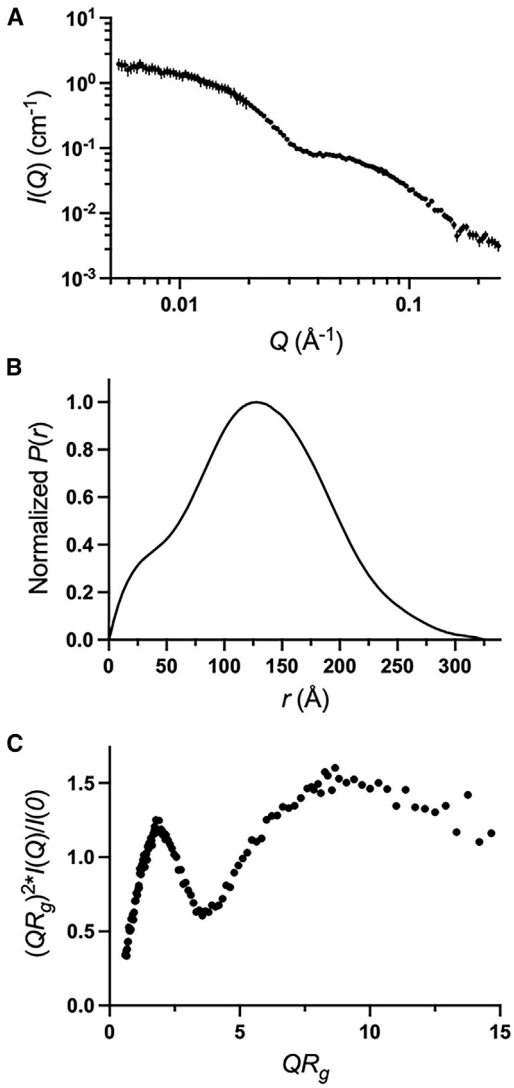

FIGURE 2 Solution scattering of the flexible SiR dodecamer. (*A*) SANS profile of SiR with plateaus at low and middle Q regions and smooth waning into high Q. Error bars represent the standard deviation of $I(Q)$ which is derived via propagating the square root of the total neutron counts through the different data reduction steps. (*B*) SiR's $P(r)$ plot transformed from scattering data in (*A*) shows an extended decay to D_{max}. (*C*) Dimensionless Kratky plot of the scattering data shows SiR's globularity and a degree of flexibility.

Analysis of reconstituted D-SiR

In vitro reconstitution produced dodecameric D-SiR ($\alpha_8\beta_4$) from SiRFP (α_8) and D-SiRHP (β) for analysis by NCV. AUC, SEC, SDS-PAGE, and spectroscopic analyses (Table S2; Figs. 3 and S3) confirm that reconstituted SiR assembles with stoichiometry comparable with both SiR formed by co-expression of SiRFP and SiRHP (16) and SiR purified from source (10). The sedimentation velocity scan data fit with low root-mean-square deviation (RMSD) (Table S2 and Fig. S4). Further, each specimen sedimented with a well-defined peak in their sedimentation envelopes and with expected S values for their shape and size (Fig. 3) (7). The individual components, D-SiRHP and SiRFP, sedimented at 4.8 and 14.1 S, respectively. Reconstituted D-SiR sedimented at 17.5 S, in agreement with the published value of the native complex purified from source (10). AUC MW and f/f_0 values for each specimen were

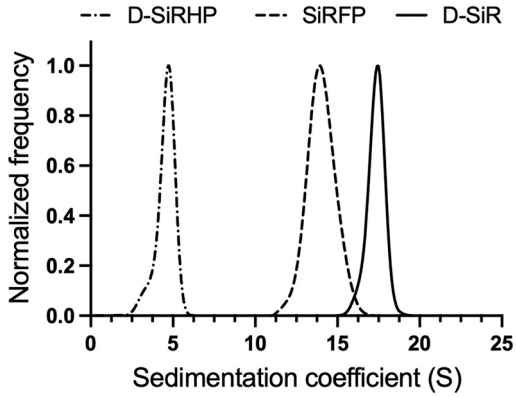

FIGURE 3 Sedimentation velocity AUC of reconstituted D-SiR and its components. Sample envelopes exhibit single peaks, indicating the purity of their preparations. Reconstituted D-SiR's sedimentation value agrees with published values for source-purified SiR (10).

as expected (Table S2). Therefore, samples prepared as described above were used for SANS measurements.

Co-expressed SiR, reconstituted, hydrogenated SiR (H-SiR), and D-SiR each scattered similarly (Fig. S5) and were unaffected by concentration or structure factor effects (Fig. S6). The calculated SANS MW for D-SiR of 839 kDa agreed with its theoretical MW of 826 kDa (1.6% difference; Table 1). The theoretical MWs for co-expressed and reconstituted specimens differ slightly due to varying his-tag linker lengths on SiRFP in the different expression constructs. SANS analyses of D-SiR and SiR describe a dodecameric complex and agree with the long-hypothesized $\alpha_8\beta_4$ subunit stoichiometry (10).

Contrast variation offers insights on the positions and centers of mass of SiR components

An NCV series was measured for D-SiR at five H_2O:D_2O ratios (contrast points), including measurements at each subunit's CMP as well as full contrast: 0%, 20%, 41%, 86%, and 100% (Fig. 4 *A*). R_g and D_{max} for the complex at each contrast point vary depending on which component is contributing more to the signal under those conditions, with D-SiRHP scattering isolated at 41% D_2O (DSiR41, SiRFP contrast matched), SiRFP scattering isolated at 86% D_2O (DSiR86, D-SiRHP contrast matched), and D-SiR's total scattering at 0% D_2O (DSiR0, full contrast; Table 1; Fig. 4 *A*). Guinier analyses confirmed each specimen was free from aggregation (Fig. S1 *B–F*). A Stuhrmann plot derived from D-SiR's NCV series showed the quadratic relationship between R_g^2 and inverse contrast ($\Delta\overline{\rho}^{-1}$), suggesting an asymmetric dodecamer (Fig. 4 *B*) (37). Further, the peak maximum of the fitted polynomial (corresponding to the positive value of α; Table 2) suggested that the component with higher SLD (D-SiRHP) is at the periphery of the complex (Fig. 4 *B*), whereas SiRFP is central to the complex. Additionally, Stuhrmann analysis showed the *D* between each component's COM is 104 Å and calculated R_g values for SiRFP and D-SiRHP, which are 74 and 105 Å, respectively (Table 2). The R_m of D-SiR was 98.3 Å, consistent with its experimental R_g (Tables 1 and 2). Finally, the PAT was used to obtain *D* and R_g parameters that agreed with the Stuhrmann and experimental values (Table 2).

Decomposition of D-SiR's NCV data series revealed its composite scattering functions, which, along with respective $P(r)$ function calculations, matched those of the experimental data (Table 2; Figs. S7 and S8) (37). Addition of the composite scattering profiles yielded a scattering function, $P(r)$, and associated R_g and D_{max} values that reflected those of the whole complex (Table 2; Figs. S7 *B* and S8 *A*). The cross-term's $P(r)$ function represents the interatomic distances between atoms in SiRFP and D-SiRHP, which had a peak at r = 146 Å and a shoulder centered over r at approximately 70 Å (Fig. S8 *A*). These values agree with each component's *D* value, further supporting the interpretation that SiR is an asymmetric complex (Table 2).

Following NCV analysis of D-SiR, a similar NCV series was measured on a 1:1 αβ complex of monomeric SiRFP (SiRFP-60) and D-SiRHP (SiRFP-60/D-SiRHP) to

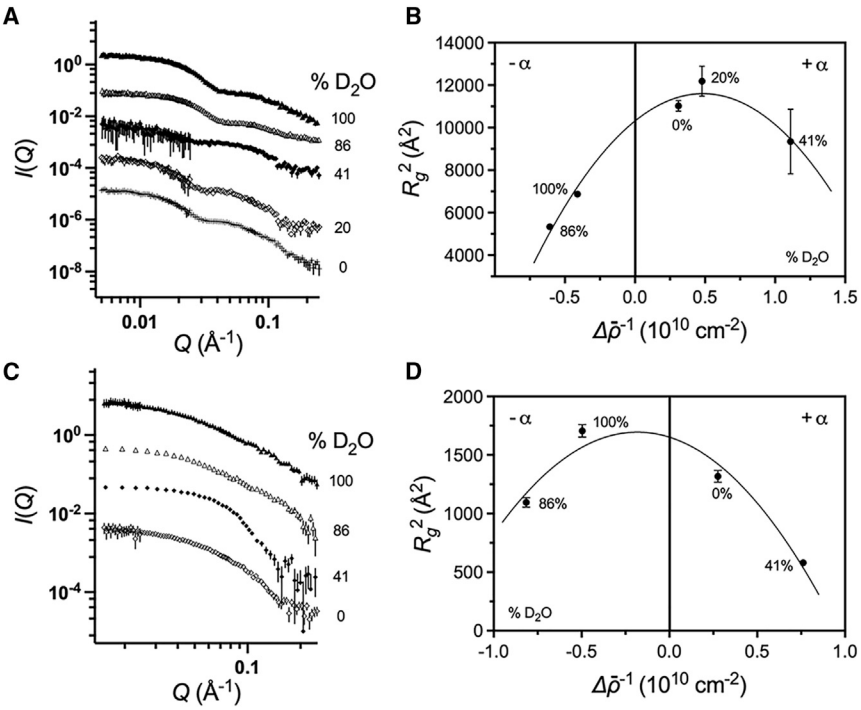

FIGURE 4 NCV analysis of D-SiR reveals subunit COM and positions in the complex. (*A*) NCV series of D-SiR in buffers with varying percentages of D_2O. Error bars are defined as in Fig. 2 *A*. (*B*) Stuhrmann plot obtained from the scattering in (*A*). (*C*) Contrast series on SiRFP-60/D-SiRHP with varying percentages of D_2O. (*D*) Stuhrmann plot obtained from the scattering in (*C*). Data in (*A*) and (*C*) were rescaled for clarity.

TABLE 2 Structural parameters for the components of D-SiR complexes

Components		SiRFP	D-SiRHP	Complex
Contrast	$\Delta\rho$ (10^{10} cm^{-2})	2.42–5.67f_{D2O}[b]	4.87–5.60f_{D2O}	
Experimental	R_g (Å)	73.0 ± 0.7	96.7 ± 7.9	105 ± 1.2
	D_{max} (Å)	220	285	315
Stuhrmann analysis	R_g (Å)	74.0 ± 0.8	105.2 ± 8.6	
	R_m (Å)			98.3 ± 1.4
	D (Å)[a]			104 ± 17
	A			5186 ± 441
	B			3326 ± 1079
Parallel axis theorem	R_g (Å)	73.9 ± 0.9	104.9 ± 8.9	
	D (Å)			105.3 ± 17
Composite scattering functions	R_g (Å)	73.0 ± 0.6	93.9 ± 9.7	101.3 ± 2.6
	D_{max} (Å)	210	285	315

[a]D is the separation of the centers of mass.
[b]f_{D2O} is the D_2O fraction in the solvent.

determine the separation between the heterodimer components' COMs (Fig. 4 *C*; Tables 1 and 3). Guinier analyses showed the heterodimer was free of aggregation throughout the NCV series (Fig. S1 *G–J*). A Stuhrmann plot from SiRFP-60/D-SiRHP's NCV series revealed the fitted polynomial had a peak maximum at negative α, indicating that the component with lower SLD (SiRFP-60) is extended away from the component with the higher SLD (SiRHP), toward the outside of the complex (Table 3; Fig. 4 *D*). Stuhrmann analysis showed the complex's D value was 56.9 Å, with associated R_g calculations yielding 34.7 and 21.4 Å for SiRFP-60 and D-SiRHP, respectively (Table 3). The R_g values agreed with experimentally determined values and the distance between COM agreed with those calculated from the subunit assignments in SiRFP-60/SiRHP's solution structure (7). The R_m of the heterodimer was 40.6 Å, which agrees with the R_g of both its own experimental data and that of the previously published, hydrogenated heterodimer (Table 3) (7). Further, the SANS MW of reconstituted SiRFP-60/D-SiRHP was 136 kDa, close to the expected value (Table 1). Again, PAT was used to obtain D and R_g

TABLE 3 Structural parameters for the components of SiRFP-60/D-SiRHP complexes

Components		SiRFP-60	D-SiRHP	Complex
Contrast	$\Delta\rho$ (10^{10} cm^{-2})	2.42–5.67f_{D2O}[b]	4.87–5.60f_{D2O}	
Experimental	R_g (Å)	33.1 ± 0.5	24.1 ± 0.6	36.3 ± 0.7
	D_{max} (Å)	124	66	134
Stuhrmann analysis	R_g (Å)	34.7 ± 1.9	21.4 ± 2.9	
	R_m (Å)			40.6 ± 2.4
	D (Å)[a]			56.9 ± 8.1
	A			−436 ± 114
	B			1290 ± 367
Parallel axis theorem	R_g (Å)	34.7 ± 2.0	20.6 ± 3.2	
	D (Å)			57.5 ± 8.2

[a]D is the separation of the centers of mass.
[b]f_{D2O} is the D_2O fraction in the solvent.

parameters that were similar to both Stuhrmann and experimental values (Table 3).

SiRFP compacts upon SiR assembly

To investigate the effects of dodecamer assembly on SiRFP's solution structure, SANS of SiRFP was measured at full contrast (100% D_2O) for comparison with SiRFP in the context of reconstituted D-SiR (DSiR86; Table 1; Fig. 5 *A*). Each dataset was free from aggregation, as shown through Guinier analyses (Fig. S1 *E* and *K*). Compared with octameric SiRFP alone, DSiR86 appeared to compact within the dodecamer, measured by a reduction in R_g from 80.8 to 73.0 Å. Further, the $P(r)$ functions were similar in shape except that DSiR86's D_{max} contracted from 260 to 220 Å when bound to D-SiRHPs (Figs. 5 *B* and S2 *B* and *C*). Kratky analyses showed that SiRFP possesses flexibility that does not diminish upon dodecamer assembly (Fig. S9 *A*) and likely arises from the disordered regions of its N-terminal octamerization domain and flexible linkers (7,17). Kratky analysis of SiRFP-60 monomer and its heterodimer with SiRHP also exhibited features consistent with flexibility, likely arising from the linker connecting flavin-binding domains, whereas the plot of the heterodimer possessed an additional peak at low QR_g due to its bilobed structure (Fig. S9 *B*). The SANS MW for SiRFP was 578 kDa, close to the theoretical MW of the his-tagged protein, 571 kDa (1.2% difference), confirming its oligomeric state as an octamer of flavoprotein subunits (Table 1). Additionally, the composite scattering function for the SiRFP component of D-SiR and its associated $P(r)$ overlapped with that of DSiR86 (Figs. S7 *C* and S8 *B*). Ab initio envelopes describing the low-resolution structures of SiRFP octamer and DSiR86 reflect compaction of the octamer upon binding SiRHP (Fig. 5 *B–D*), echoing the change in structure of SiRFP-60 upon binding SiRHP in the minimal dimer (7). DSiR86 further showed individual lobes extending outward from a centralized domain (Fig. 5 *D*). The theoretical scattering of these low-resolution envelopes agreed with their experimental data (Fig. S10 *A* and *B*). Additionally, the theoretical S and R_g values of SiRFP's model were determined to be 14.4 S and 83.9 Å by US-SOMO, respectively, compared with the sedimentation velocity AUC- and SANS-determined values of 14.1 S and 80.8 Å (Tables 1 and S2; Fig. 3).

SiRHP positioning in the SiR dodecamer

In the absence of a structure for the whole SiR dodecamer, we do not know the impact of SiRFP's oligomerization or other inter-subunit interactions on how SiRHP is positioned within the complex, given that SiRHP does not oligomerize when isolated from the dodecameric complex or when expressed independently (10,25,67). To assess the location of SiR's SiRHP subunits, we measured SANS of D-SiR at SiRFP's CMP (41% D_2O, DSiR41) as well as monomeric

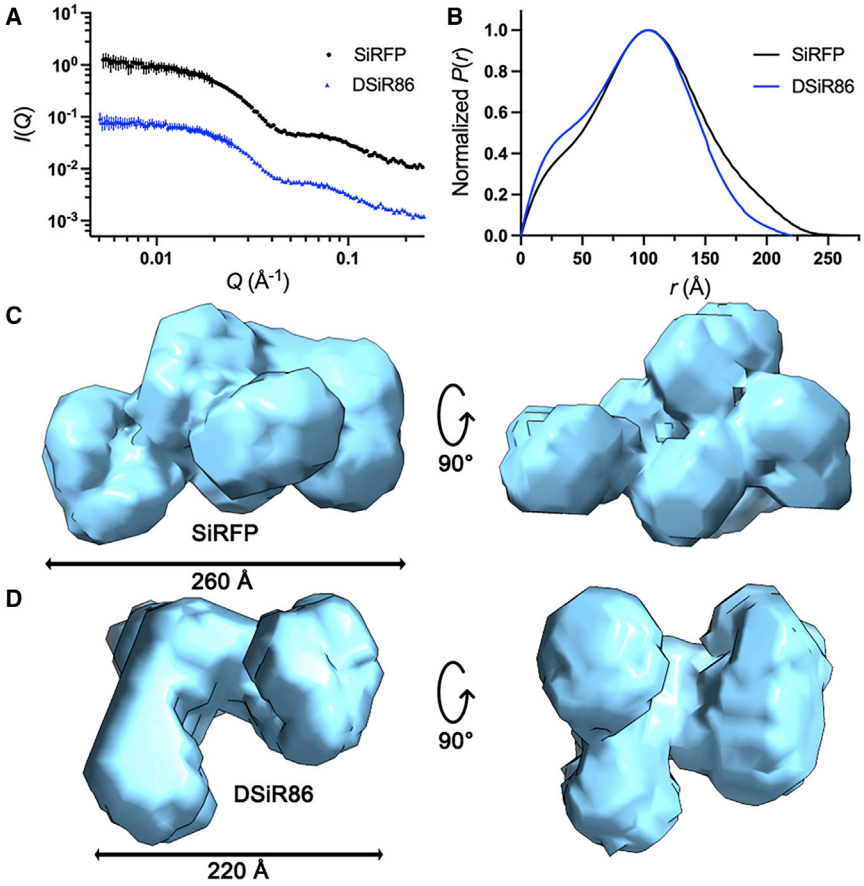

FIGURE 5 SiRFP shows compaction upon binding SiRHP. (*A*) Scattering profiles of SiRFP and DSiR86. Data were rescaled for clarity. Error bars are defined as in Fig. 2 *A*. (*B*) *P*(*r*) plots calculated from the scattering in (*A*) showing a reduced D_{max} of DSiR86 compared with SiRFP. (*C*) Envelope of SiRFP with a D_{max} of 260 Å, scale bar in solid black. (*D*) Envelope of DSiR86's overall structure with a D_{max} of 220 Å, scale bar in solid black.

SiRHP at full contrast (100% D_2O; Fig. 6 *A*). These scattering data were free from aggregation, according to Guinier analyses (Fig. S1 *D* and *L*). Analysis of SiRHP's scattering data yielded an R_g and D_{max} of 23.3 and 72 Å, respectively, as expected from this well-characterized metalloenzyme (Table 1) (7,16,26). Alternatively, analysis of DSiR41

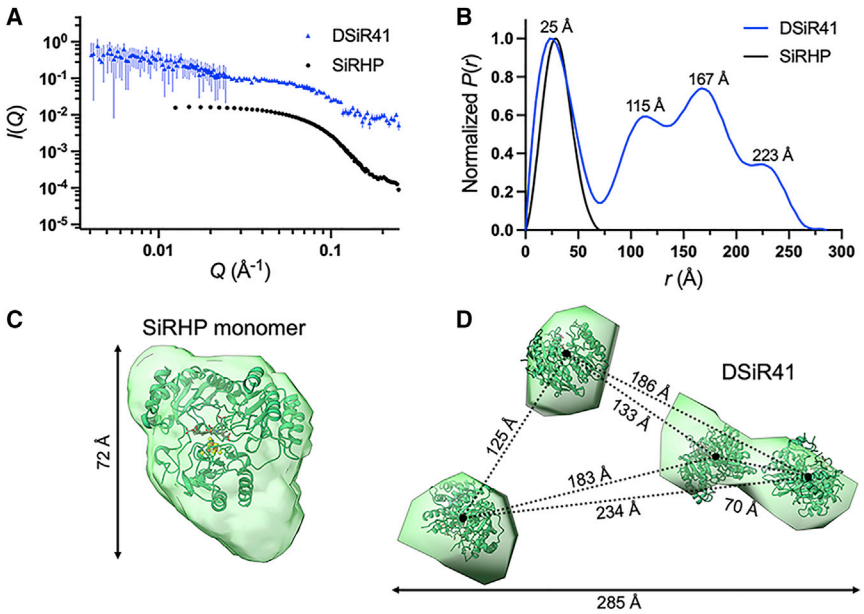

FIGURE 6 Scattering of monomeric and complexed SiRHP. (*A*) SANS profiles of SiRHP and DSiR41. Data were rescaled for clarity. Error bars are defined as in Fig. 2 *A*. (*B*) *P*(*r*) plot showing peaks of monomeric SiRHP and of DSiR41's SiRHPs within the dodecamer. (*C*) Ab initio envelope (*green density map*) of the isolated SiRHP monomer (D_{max} = 72 Å) with its crystal structure docked (*green ribbon*, PDB: 1AOP). (*D*) Ab initio envelope (*green density map*) calculated for DSiR41 (D_{max} = 285 Å) with four SiRHPs docked, as calculated by rigid body modeling (*green ribbons*). The measured distances between each subunit's COM agree with the distance distributions shown in (*B*). Scale bars are solid (D_{max}) or dotted (COM *D* values).

gave an R_g and D_{max} of 96.7 and 285 Å, respectively, indicating that SiRHP scatters as a large structure within the dodecamer. The $P(r)$ function of DSiR41 exhibited four peaks, with the peak at lowest r values (approximately 25 Å) overlapping with the single peak of the $P(r)$ for monomeric SiRHP's intra-subunit distances (Figs. 6 *B* and S2 *D* and *E*). The three other peaks in the $P(r)$ function center over r values of 115, 167, and 223 Å. These distance distributions are suggestive of inter-subunit distances between the four SiRHP subunits in the complex. Additionally, the composite scattering function for the SiRHP component of D-SiR and its associated $P(r)$ overlapped with those from DSiR41's experimental data (Table 2; Figs. S7 *D* and S8 *C*).

Ab initio modeling of monomeric SiRHP's scattering yielded an envelope function of the subunit's monomeric solution structure (Fig. 6 *C*) whose theoretical scattering matched the experimental data (Fig. S10 *C*). The theoretical S and R_g values of this model were determined to be 4.9 S and 24.9 Å, respectively, compared with the sedimentation velocity AUC- and SANS-determined values for monomeric hemoprotein of 4.8 S and 25.9 Å (Table S2). Alternatively, the ab initio envelope function for DSiR41 contained disjointed densities that are the shape of four separate SiRHP subunits, with the maximal spacing of densities aligned with the calculated $P(r)$ and D_{max} (Fig. 6 *B* and *D*). Together, each independent density or pair of densities readily accommodates four SiRHP subunits, with two isolated densities that are the approximate size of individual subunits and one larger envelope that fits two proximal SiRHPs. The theoretical scattering of the low-resolution envelope fit the experimental data (Fig. S10 *D*). To support this model, rigid body fitting of DSiR41's scattering data placed four SiRHPs with inter-subunit distances and relative positioning that guided their docking into DSiR41's ab initio envelope function (Fig. 6 *D*) (59). The resulting theoretical scattering, calculated during rigid body modeling, fit the experimental data with $\chi^2 = 1.04$ (Fig. S11). Distance measurements between each of the SiRHPs' COMs as placed from rigid body modeling of DSiR41, calculated in ChimeraX (61), agreed with the distance distribution peaks in the $P(r)$ plot of DSiR41 (Fig. 6 *B* and *D*).

An overall map of the complex

The full-contrast measurement of D-SiR in hydrogenated buffer (0% D_2O, DSiR0) was modeled to obtain a low-resolution map of the entire complex (Fig. 7 *A*). The resulting envelope resembled a combination of those obtained from modeling DSiR86 and DSiR41, with a centralized SiRFP octamer and peripheral SiRHP subunits that make up an asymmetric complex. Placing the SiRFP and SiRHP components with their COMs separated by 104 Å, as calculated from Stuhrmann analysis, combined to complete a complex whose structure aligned with the model of the dodecameric complex. Validation statistics showed convergence of the envelope's features and theoretical scattering that fit the experimental data (Figs. S2 *F* and S10 *E*). The theoretical S and R_g values of this model were determined to be 16.8 S and 108 Å, respectively, compared with the experimentally determined values of 17.5 S and 105 Å (Table 1 and S2).

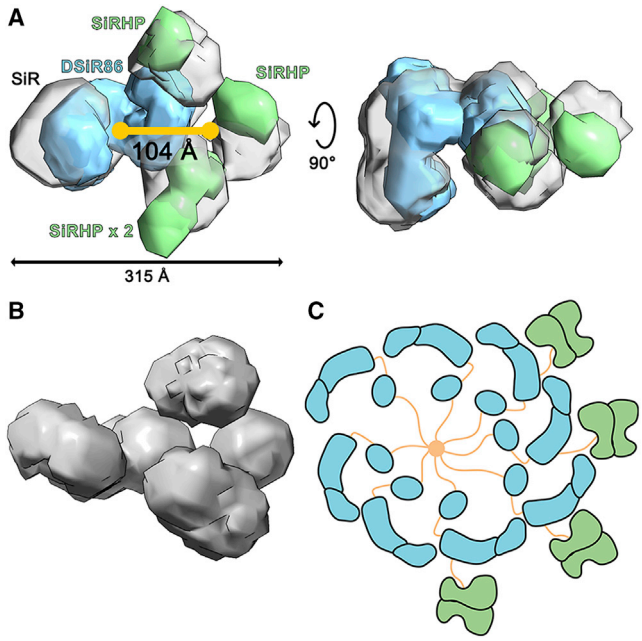

FIGURE 7 Overall map of SiR. (*A*) Superimposed ab initio models of DSiR41 (*green*), DSiR86 (*blue*), and DSiR0 (*transparent gray*). The overall complex is asymmetric, with a D_{max} of 315 Å, and each component's COM separated by 104 Å. Scale bars are black (D_{max}) or yellow (COM *D* value). (*B*) Ab initio modeling of the density based on the combined scatter from DSiR0, DSiR20, and DSiR41. (*C*) Based on SANS and AUC parameters, models of the scattering functions, and analysis the NCV series, we propose a sided subunit arrangement in SiR; however, other arrangements could also explain this asymmetric complex (Fig. 1 *B*).

We tested this proposed assignment of densities by then calculating an ab initio model combining the information from three scattering experiments measured at different contrasts (DSiR0, DSiR20 [Fig. S2 *G*], and DSiR41) using a new implementation of DENSS, DENSS-Multiple (58). After refinement against the total scatter, the resulting map closely resembled the model calculated from DSiR0 as well as our assignment of the densities to each subunit (Fig. 7 *B*).

DISCUSSION

Initial structural characterization of solution-state SiR

Structures of SiR's monomeric subunits were determined by X-ray crystallography, and their 1:1 heterodimer solution structure was visualized at low resolution by SANS (7,14,26,28). However, structural characterization of higher-order assemblies of SiR is lacking, so we do not know the arrangement of SiR's subunits to shed light on possible

pathways for its *cis*/*trans* electron transfer (16,17). Specifically, questions about whether the complex is distributed symmetrically or not, whether SiRHP is centrally or peripherally located, and the impact of dodecamer assembly on the organization and conformation of SiRFP are unresolved. To address these questions, we measured the neutron scattering of higher-order SiR complexes and its components, including co-expressed SiR, reconstituted D-SiR, octameric SiRFP, and monomeric SiRHP.

The structural parameters of SiR determined from SANS show that the extended dodecamer has an R_g and D_{max} of 101.5 and 325 Å, respectively (Table 1). SiR's large size sets it apart from similar oxidoreductases that do not have excess reductase subunits and only catalyze one or two electron transfer reactions, and therefore do not need a high local density of electron donors (3,21,68). In SiR, three NADPH molecules are needed to deliver six electrons through SiRFP to the active site in SiRHP, which potentially explains the stoichiometric mismatch of oxidase and reductase subunits in the dodecameric holoenzyme. MW determination based on SANS and sedimentation velocity AUC indicate the complex adopts the $\alpha_8\beta_4$ stoichiometry, confirming the original designation of the complex as a dodecamer (10) and without equal subunit stoichiometry as others have posited (25) (Tables 1 and S2; Fig. 3). Further, comparing Kratky analyses of octameric SiRFP (Fig. S9 *A*) with monomeric SiRFP-60 (7,14) (Fig. S9 *B*) or Kratky analyses of dodecameric SiR (Fig. 2 *C*) with that of the heterodimer (Fig. S9 *B*) suggests that the N-terminal octamerization domain imparts additional flexibility beyond that stemming from the linker between the Fld and FNR domains. The flexibility identified in the Kratky analysis of SiR's solution scattering (Fig. 2 *C*), as predicted by sequence analysis (17), suggests a role for large-scale conformational changes in delivering three independent electron transfer interactions between a reduced SiRFP and SiRHP.

Contributions of each subunit to the dodecameric structure

Reconstituted D-SiR was characterized with AUC and SANS to obtain a sedimentation envelope whose peak S value is consistent with published values and an MW that agrees with theoretical values, confirming that the assembled complex was formed properly and is a dodecamer (Tables 1 and S2; Figs. 3 and 4 *A*) (10). Additionally, SANS of reconstituted D-SiR yielded structural parameters that agree with the co-expressed form's SANS MW, R_g, and D_{max} (Table 1). The SANS contrast points for D-SiR included measurements at full contrast (DSiR0; Fig. 4 *A*), at the CMPs of both subunits (DSiR86 and DSiR41; Figs. 5 *A* and 6 *A*), as well as measurements on either side of their respective CMPs (DSiR20 and DSiR100; Table 1; Fig. 4 *A*). From analyzing these measurements, the scattering shows that the COMs for SiRFP and SiRHP components are separated by 104 Å in the dodecamer and demonstrate that the complex is not symmetric, despite the potential for at least four-fold symmetry (Table 2; Figs. 1, 4 *B*, and 7). The four SiRHP subunits are at the periphery of the complex where they bind independently of one another.

SiR's $P(r)$, with a peak around 128 Å and a small shoulder at low r, is indicative of a non-spherical particle that has two components, one with long-scale interatomic distances and a secondary component that is considerably smaller. In our model, the longest-scale distances correspond to vectors spanning the whole complex, whereas the smaller distances stem from the independent subunits. Decomposition of D-SiR's scattering into its composite scattering functions further revealed the scattering of each subunit (Fig. S7), which agreed with measurements at the contrast points isolating their scattering contributions (Figs. 5 *A*, 6 *A*, S7, and S8). The cross-term function, whose $P(r)$ shows the distance distributions between SiRFP and SiRHP, had an r value peak at 146 Å and a shoulder at approximately 70 Å (Fig. S8 *A*), skewing larger than the $P(r)$ for the whole complex (Figs. 2 *B* and S2 *A*) because it only captures those distances between the peripheral SiRHP subunits and the larger octameric SiRFP, not those within the individual SiRHP subunits. Importantly, D_{max} values determined from orthogonal experiments agree, putting the maximum dimension of the complex at approximately 315 Å (Tables 1 and 2).

SiRHP binding affects SiRFP's structure

An NCV series was measured on a SiRFP-60/D-SiRHP heterodimer in the oxidized state, whose subsequent analysis showed each subunit's COM to be separated by 56.9 Å and that SiRFP-60's extended structure, rather than SiRHP, is toward the complex's periphery (Table 3; Fig. 4 *C* and *D*). These observations show that SiRFP's Fld domain is distally located relative to the complex's overall COM and is positioned to enable either intermolecular, or *trans*, electron transfer to another FNR domain or oxidase partner within the dodecamer, and agrees with the domain assignments within the heterodimer's previously published solution structure (7).

Similar to DSiR86, purified octameric SiRFP possesses an extended structure with a degree of flexibility stemming from the intrinsic disorder of its octamerization domain and the eight flexible, 30-residue-long linkers that tether domains within its subunits (Figs. 5 *B* and S9 *A*). SANS MW and sedimentation coefficient values for SiRFP are consistent with an α_8 complex (Table 1; Fig. 3). Here, we show that binding of SiRHP to octameric SiRFP imparts a rearrangement in SiRFP's structure to a more compact state, possibly as a result of the same interactions that affect SiRFP's conformation in its heterodimer form (Table 1; Fig. 5 *B–D*) (7). A compact SiRFP may lend itself to a *cis*

electron transfer between neighboring SiRFP subunits. Further modeling SiRFP monomers into the envelope of the octameric scattering profile proved challenging because of the unresolved structure of the N-terminal octamerization domain.

SiRHP adopts asymmetric positions in the dodecamer

SiR is not a symmetric oligomer, as shown by the 104 Å separation between the COMs of SiRFP and SiRHP. Further, the f/f_0 values for SiRFP and SiR, which deviate from the expected value of 1.2 for a hydrated sphere (69), support that these are elongated, asymmetric complexes unlike the more globular SiRHP (Table S2). When expressed in isolation or when dissociated from the dodecamer, SiRHP is monomeric (Table 1; Figs. 3 and 6) (10,67). Nevertheless, SiRHP within the dodecamer scatters with significantly larger structural values than expected for a particle with the size and contrast of monomeric SiRHP (Tables 1 and 2; Fig. 6). Thus, SiRHP's uneven distribution around the COM of the dodecamer and its position at the periphery of the complex is feasible because assembly does not depend on SiRHP oligomerization. Interestingly, a Guinier fit in the middle Q region ($0.02 < Q < 0.06$) of DSiR41's scattering profile, reflecting the reciprocal space length scales of individual SiRHP subunits, satisfies QR_g limits and yields an R_g of 21 Å (Fig. 6 *A*), similar to the compact form of SiRHP observed in the SiRFP-60/D-SiRHP heterodimer (7) but in contrast to the less compact, free SiRHP monomer (Tables 1 and 3; Figs. 4 *C* and 6 *B* and *C*). SiRHP's compaction upon binding SiRFP is likely due to its intrinsically disordered, extended N terminus rearranging to mediate inter-subunit contacts (7,17).

Two competing models could explain the asymmetric distribution of SiRHP across the dodecamer. In one, the monomers bind to the same side of the SiRFP octamer at adjacent SiRFP subunits (Fig. 1 *B*). The close proximity of two of the four SiRHP monomers does not preclude their transient association playing a role in their positioning within the complex (Fig. 6). Further, higher-order structures of SiRHP form when the protein is expressed in its apo form, supporting the possibility of a transient interaction in the complex (16). Finally, this arrangement seems to describe the positions of the four SiRHP monomers when visualized down the long axis of the elongated complex (Fig. 7).

In the other model, SiRHP could evenly distribute on some subset of SiRFP subunits, for example on every other subunit or every other pair of two, perhaps driven by steric clashes between too-close SiRHPs and with the asymmetry derived from SiRFP's well-characterized conformational flexibility (Fig. 1 *B*) (7,17,28). In this model, close proximity of two of the SiRHP subunits suggests that they are being brought together through their interactions with an asymmetric SiRFP. However, modeling of the complex with a 104 Å separation between COMs indicates the former model as more likely, with SiRHP binding to the same side of SiRFP at adjacent positions (Fig. 7 *C*). Given the flexibility of the complex, however, we cannot preclude the other options.

CONCLUSIONS

The studies described here deliver an initial structural characterization of SiR's higher-order complex that informs its behavior in solution as a result of assembly into native dodecamer. We systematically probed the components of SiR alone, as assembled through co-expression, and as a reconstituted specimen using SANS. Analysis of SiR's structural parameters, an NCV series, and modeling support several conclusions that inform our understanding of its dodecameric structure. First, the posited $\alpha_8\beta_4$ stoichiometry of co-expressed or reconstituted SiR was confirmed through both solution scattering and AUC (Tables 1 and S2; Fig. 3). Second, NCV revealed the complex to be asymmetric because the COMs of each subunit are separated by over 100 Å with SiRHP at the periphery (Table 2; Fig. 4). Third, SiRFP compacts upon dodecamer assembly, bringing SiRFP and SiRHP subunits closer to enable access of reductases with each other or with their oxidase partners (Fig. 5). Finally, SiRHP adopts multiple positions with varying distances from each other, in contrast to an even inter-subunit distancing suggestive of a symmetric arrangement about the complex (Figs. 6 *B* and S8). Ab initio and rigid body modeling converge on the same placement of SiRHPs in the complex, which also agree with distance distribution calculations (Fig. 6 *B* and *D*). To our knowledge, these observations enable the first mapping of SiR's overall structure and are informed upon by its low-resolution envelope (Fig. 7). In summary, the insights presented here show that dodecamer assembly brings a stoichiometric excess of SiRFP to SiRHP subunits to increase the local density of reducing equivalents that are candidates for transfer to SiRHP. With SiRHP peripherally located in an asymmetric complex with compacted SiRFP, there is ample potential for redundant electron transfer pathways between reductase and oxidase subunits. These insights will also aid in the design of future structure-function studies of SiR, as well as other multicomponent complexes possessing flexibility and recalcitrance to static structural techniques.

SUPPORTING MATERIAL

Supporting material can be found online at https://doi.org/10.1016/j.bpj.2022.04.021.

AUTHOR CONTRIBUTIONS

D.T.M., N.W., G.N., C.B.S., and M.E.S. performed SANS experiments and analyzed data. D.T.M, G.N., C.B.S., and M.E.S. designed SANS

experiments. D.T.M., N.W., and P.S.R. performed biochemistry experiments and analyzed data. D.T.M. and M.E.S. designed biochemistry experiments. D.T.M. and K.L.W. designed and performed deuteration experiments. M.E.S. designed the project and wrote the manuscript together with D.T.M. All authors reviewed, approved, and contributed to the final version of the manuscript.

DECLARATION OF INTEREST

The authors declare no competing interests.

ACKNOWLEDGMENTS

We would like thank Andrew Whitten, Jill Trewhella, Shuo Qian, and Jake Sumner for helpful discussions regarding the analysis of NCV data and Tristan Dilbeck for careful reading of the manuscript. A portion of this research used resources at the Spallation Neutron Source, a DOE Office of Science user facility operated by the Oak Ridge National Laboratory. The Office of Biological and Environmental Research also supported work at the ORNL Center for Structural Molecular Biology. This work was supported by National Science Foundation grants MCB1856502 and CHE1904612 to M.E.S.

REFERENCES

1. Wakil, S. J. 1989. Fatty acid synthase, a proficient multifunctional enzyme. *Biochemistry.* 28:4523–4530. https://doi.org/10.1021/bi00437a001.
2. Sousa, J. S., E. D'Imprima, and J. Vonck. 2018. Mitochondrial respiratory chain complexes. *Subcell Biochem.* 87:167–227. https://doi.org/10.1007/978-981-10-7757-9_7. https://www.ncbi.nlm.nih.gov/pubmed/29464561.
3. Campbell, M. G., B. C. Smith, …, M. A. Marletta. 2014. Molecular architecture of mammalian nitric oxide synthases. *Proc. Natl. Acad. Sci. U S A.* 111:E3614–E3623. https://doi.org/10.1073/pnas.1413763111. https://www.ncbi.nlm.nih.gov/pubmed/25125509.
4. Kastritis, P., L. Kastritis, …, A.-C. Gavin. 2018. Enzymatic complexes across scales. *Essays Biochem.* 62:501–514. https://doi.org/10.1042/ebc20180008.
5. Freeman, S. L., A. Martel, …, G. C. Roberts. 2018. Solution structure of the cytochrome P450 reductase-cytochrome c complex determined by neutron scattering. *J. Biol. Chem.* 293:5210–5219. https://doi.org/10.1074/jbc.RA118.001941. https://www.ncbi.nlm.nih.gov/pubmed/29475945.
6. Yokom, A. L., Y. Morishima, …, D. R. Southworth. 2014. Architecture of the nitric-oxide synthase holoenzyme reveals large conformational changes and a calmodulin-driven release of the FMN domain. *J. Biol. Chem.* 289:16855–16865. https://doi.org/10.1074/jbc.M114.564005. https://www.ncbi.nlm.nih.gov/pubmed/24737326.
7. Murray, D. T., K. L. Weiss, …, M. E. Stroupe. 2021. Small-angle neutron scattering solution structures of NADPH-dependent sulfite reductase. *J. Struct. Biol.* 213:107724. https://doi.org/10.1016/j.jsb.2021.107724.
8. Siegel, L. M., M. J. Murphy, and H. Kamin. 1973. Reduced nicotinamide adenine dinucleotide phosphate-sulfite reductase of enterobacteria. I. The Escherichia coli hemoflavoprotein: molecular parameters and prosthetic groups. *J. Biol. Chem.* 248:251–264. https://www.ncbi.nlm.nih.gov/pubmed/4144254.
9. Siegel, L. M., P. S. Davis, and H. Kamin. 1974. Reduced nicotinamide adenine dinucleotide phosphate-sulfite reductase of enterobacteria. 3. The Escherichia coli hemoflavoprotein: catalytic parameters and the sequence of electron flow. *J. Biol. Chem.* 249:1572–1586. https://www.ncbi.nlm.nih.gov/pubmed/4150390.
10. Siegel, L. M., and P. S. Davis. 1974. Reduced nicotinamide adenine dinucleotide phosphate-sulfite reductase of enterobacteria. IV. The Escherichia coli hemoflavoprotein: subunit structure and dissociation into hemoprotein and flavoprotein components. *J. Biol. Chem.* 249:1587–1598. https://www.ncbi.nlm.nih.gov/pubmed/4150391.
11. Xia, C., S. P. Panda, …, J. J. P. Kim. 2011. Structural basis for human NADPH-cytochrome P450 oxidoreductase deficiency. *Proc. Natl. Acad. Sci. U S A.* 108:13486–13491. https://doi.org/10.1073/pnas.1106632108. https://www.ncbi.nlm.nih.gov/pubmed/21808038.
12. Zhang, H., A. L. Yokom, …, Y. Osawa. 2018. The full-length cytochrome P450 enzyme CYP102A1 dimerizes at its reductase domains and has flexible heme domains for efficient catalysis. *J. Biol. Chem.* 293:7727–7736. https://doi.org/10.1074/jbc.RA117.000600. https://www.ncbi.nlm.nih.gov/pubmed/29618513.
13. Olteanu, H., and R. Banerjee. 2001. Human methionine synthase reductase, a soluble P-450 reductase-like dual flavoprotein, is sufficient for NADPH-dependent methionine synthase activation. *J. Biol. Chem.* 276:35558–35563. https://doi.org/10.1074/jbc.M103707200. https://www.ncbi.nlm.nih.gov/pubmed/11466310.
14. Tavolieri, A. M., D. T. Murray, …, M. E. Stroupe. 2019. NADPH-dependent sulfite reductase flavoprotein adopts an extended conformation unique to this diflavin reductase. *J. Struct. Biol.* 205:170–179. https://doi.org/10.1016/j.jsb.2019.01.001. https://www.ncbi.nlm.nih.gov/pubmed/30654136.
15. Murphy, M. J., L. M. Siegel, …, D. Rosenthal. 1973. Reduced nicotinamide adenine dinucleotide phosphate-sulfite reductase of enterobacteria. II. Identification of a new class of heme prosthetic group: an iron-tetrahydroporphyrin (isobacteriochlorin type) with eight carboxylic acid groups. *J. Biol. Chem.* 248:2801–2814. https://www.ncbi.nlm.nih.gov/pubmed/4144546.
16. Askenasy, I., J. M. Pennington, …, M. E. Stroupe. 2015. The N-terminal domain of Escherichia coli assimilatory NADPH-sulfite reductase hemoprotein is an oligomerization domain that mediates holoenzyme assembly. *J. Biol. Chem.* 290:19319–19333. https://doi.org/10.1074/jbc.M115.662379. https://www.ncbi.nlm.nih.gov/pubmed/26088143.
17. Askenasy, I., D. T. Murray, …, M. E. Stroupe. 2018. Structure-function relationships in the oligomeric NADPH-dependent assimilatory sulfite reductase. *Biochemistry.* 57:3764–3772. https://doi.org/10.1021/acs.biochem.8b00446. https://www.ncbi.nlm.nih.gov/pubmed/29787249.
18. Freeman, S. L., A. Martel, …, G. C. K. Roberts. 2017. Orchestrated domain movement in catalysis by cytochrome P450 reductase. *Sci. Rep.* 7:9741. https://doi.org/10.1038/s41598-017-09840-8. https://www.ncbi.nlm.nih.gov/pubmed/28852004.
19. Freeman, S. L., A. Martel, …, G. C. Roberts. 2018. Solution structure of the cytochrome P450 reductase-cytochrome. *J. Biol. Chem.* 293:5210–5219. https://doi.org/10.1074/jbc.RA118.001941. https://www.ncbi.nlm.nih.gov/pubmed/29475945.
20. Iyanagi, T., C. Xia, and J. J. P. Kim. 2012. NADPH-cytochrome P450 oxidoreductase: prototypic member of the diflavin reductase family. *Arch. Biochem. Biophys.* 528:72–89. https://doi.org/10.1016/j.abb.2012.09.002. https://www.ncbi.nlm.nih.gov/pubmed/22982532.
21. Wang, M., D. L. Roberts, …, J. J. P. Kim. 1997. Three-dimensional structure of NADPH-cytochrome P450 reductase: prototype for FMN- and FAD-containing enzymes. *Proc. Natl. Acad. Sci. U S A.* 94:8411–8416. https://doi.org/10.1073/pnas.94.16.8411. https://www.ncbi.nlm.nih.gov/pubmed/9237990.
22. Huang, W. C., J. Ellis, …, G. Roberts. 2013. Redox-linked domain movements in the catalytic cycle of cytochrome p450 reductase. *Structure.* 21:1581–1589. https://doi.org/10.1016/j.str.2013.06.022. https://www.ncbi.nlm.nih.gov/pubmed/23911089.
23. Hamdane, D., C. Xia, …, L. Waskell. 2009. Structure and function of an NADPH-cytochrome P450 oxidoreductase in an open conformation capable of reducing cytochrome P450. *J. Biol. Chem.* 284:11374–11384. https://doi.org/10.1074/jbc.M807868200. https://www.ncbi.nlm.nih.gov/pubmed/19171935.
24. Xia, C., D. Hamdane, …, J. J. P. Kim. 2011. Conformational changes of NADPH-cytochrome P450 oxidoreductase are essential for catalysis and cofactor binding. *J. Biol. Chem.* 286:16246–16260. https://doi.

org/10.1074/jbc.M111.230532. https://www.ncbi.nlm.nih.gov/pubmed/21345800.

25. Zeghouf, M., M. Fontecave, and J. Coves. 2000. A simplifed functional version of the Escherichia coli sulfite reductase. *J. Biol. Chem.* 275:37651–37656. https://doi.org/10.1074/jbc.M005619200. https://www.ncbi.nlm.nih.gov/pubmed/10984484.

26. Crane, B. R., L. M. Siegel, and E. D. Getzoff. 1995. Sulfite reductase structure at 1.6 Å: evolution and catalysis for reduction of inorganic anions. *Science.* 270:59–67. https://doi.org/10.1126/science.270.5233.59.

27. Wu, J. Y., L. M. Siegel, and N. M. Kredich. 1991. High-level expression of Escherichia coli NADPH-sulfite reductase: requirement for a cloned cysG plasmid to overcome limiting siroheme cofactor. *J. Bacteriol.* 173:325–333. https://doi.org/10.1128/jb.173.1.325-333.1991. https://www.ncbi.nlm.nih.gov/pubmed/1987123.

28. Gruez, A., D. Pignol, …, J. C. Fontecilla-Camps. 2000. Four crystal structures of the 60 kDa flavoprotein monomer of the sulfite reductase indicate a disordered flavodoxin-like module 1 1Edited by R. Huber. *J. Mol. Biol.* 299:199–212. https://doi.org/10.1006/jmbi.2000.3748. https://www.ncbi.nlm.nih.gov/pubmed/10860732.

29. Haque, M. M., J. Tejero, …, D. J. Stuehr. 2018. A cross-domain charge interaction governs the activity of NO synthase. *J. Biol. Chem.* 293:4545–4554. https://doi.org/10.1074/jbc.RA117.000635. https://www.ncbi.nlm.nih.gov/pubmed/29414777.

30. Mirts, E. N., I. D. Petrik, …, Y. Lu. 2018. A designed heme-[4Fe-4S] metalloenzyme catalyzes sulfite reduction like the native enzyme. *Science.* 361:1098–1101. https://doi.org/10.1126/science.aat8474. https://www.ncbi.nlm.nih.gov/pubmed/30213908.

31. Lancaster, K. M. 2018. Revving up an artificial metalloenzyme. *Science.* 361:1071–1072. https://doi.org/10.1126/science.aau7754. https://www.ncbi.nlm.nih.gov/pubmed/30213900.

32. Hsieh, Y. C., M. Y. Liu, …, C. J. Chen. 2010. Structural insights into the enzyme catalysis from comparison of three forms of dissimilatory sulphite reductase from Desulfovibrio gigas. *Mol. Microbiol.* 78:1101–1116. https://doi.org/10.1111/j.1365-2958.2010.07390.x. https://www.ncbi.nlm.nih.gov/pubmed/21059110.

33. Oliveira, T. F., E. Franklin, …, M. Archer. 2011. Structural insights into dissimilatory sulfite reductases: structure of desulforubidin from desulfomicrobium norvegicum. *Front. Microbiol.* 2:71. https://doi.org/10.3389/fmicb.2011.00071. https://www.ncbi.nlm.nih.gov/pubmed/21833321.

34. Törnkvist, M., G. Larsson, and S. Enfors. 1996. Protein release and foaming in Escherichia coli cultures grown in minimal medium. *Bioproc. Eng.* 15:231–237.

35. Demeler, B., and K. van Holde. 2004. Sedimentation velocity analysis of highly heterogeneous systems. *Anal. Biochem.* 335:279–288. https://doi.org/10.1016/j.ab.2004.08.039.

36. Demeler, B., and D. Scott. 2005. UltraScan - a comprehensive data analysis software package for analytical ultracentrifugation experiments. *Anal. Ultracentrifugation: Tech. Methods.* 10:210–230.

37. Whitten, A. E., S. Cai, and J. Trewhella. 2008. M*ULCh*: modules for the analysis of small-angle neutron contrast variation data from biomolecular assemblies. *J. Appl. Crystallogr.* 41:222–226. https://doi.org/10.1107/s0021889807055136.

38. Dunne, O., M. Weidenhaupt, …, V. T. Forsyth. 2017. Matchout deuterium labelling of proteins for small-angle neutron scattering studies using prokaryotic and eukaryotic expression systems and high cell-density cultures. *Eur. Biophys. J.* 46:425–432. https://doi.org/10.1007/s00249-016-1186-2. https://www.ncbi.nlm.nih.gov/pubmed/27844110.

39. Leiting, B., F. Marsilio, and J. F. O'Connell. 1998. Predictable deuteration of recombinant proteins expressed in Escherichia coli. *Anal. Biochem.* 265:351–355. https://doi.org/10.1006/abio.1998.2904. https://www.ncbi.nlm.nih.gov/pubmed/9882413.

40. White, M. R., D. M. Mitrea, …, R. W. Kriwacki. 2019. C9orf72 poly(PR) dipeptide repeats disturb biomolecular phase separation and disrupt nucleolar function. *Mol. Cell.* 74:713–728.e6. https://doi.org/10.1016/j.molcel.2019.03.019. https://www.ncbi.nlm.nih.gov/pubmed/30981631.

41. Heller, W. T., M. Cuneo, …, W. Bras. 2018. The suite of small-angle neutron scattering instruments at Oak Ridge National Laboratory. *J. Appl. Crystallogr.* 51:242–248. https://doi.org/10.1107/s1600576718001231.

42. Zhao, J. K., C. Y. Gao, and D. Liu. 2010. The extended Q -range small-angle neutron scattering diffractometer at the SNS. *J. Appl. Crystallogr.* 43:1068–1077. https://doi.org/10.1107/s002188981002217x.

43. Arnold, O., J. C. Bilheux, …, J. Zikovsky. 2014. Mantid - data analysis and visualization package for neutron scattering and μ SR experiments. *Nucl. Instrum. Methods Phys. Res. A Accel. Spectrom. Detect. Assoc. Equip.* 764:156–166. https://doi.org/10.1016/j.nima.2014.07.029.

44. Kluyver, T., B. Ragan-Kelley, …, B. Schmidt. 2016. Jupyter Notebooks-A Publishing Format for Reproducible Computational Workflows. *In* Positioning and Power in Academic Publishing: Players, Agents and Agendas. IOS Press, pp. 87–90. https://doi.org/10.3233/978-1-61499-649-1-87.

45. Wignall, G. D., and F. S. Bates. 1987. Absolute calibration of small-angle neutron scattering data. *J. Appl. Crystallogr.* 20:28–40. https://doi.org/10.1107/s0021889887087181.

46. Hopkins, J. B., R. E. Gillilan, and S. Skou. 2017. BioXTAS RAW: improvements to a free open-source program for small-angle X-ray scattering data reduction and analysis. *J. Appl. Crystallogr.* 50 (Pt 5):1545–1553. https://doi.org/10.1107/S1600576717011438. https://www.ncbi.nlm.nih.gov/pubmed/29021737.

47. Svergun, D. I. 1992. Determination of the regularization parameter in indirect-transform methods using perceptual criteria. *J. Appl. Crystallogr.* 25:495–503. https://doi.org/10.1107/s0021889892001663.

48. Trewhella, J., A. P. Duff, …, A. E. Whitten. 2017. 2017 publication guidelines for structural modelling of small-angle scattering data from biomolecules in solution: an update. *Acta Crystallogr. D Struct. Biol.* 73 (Pt 9):710–728. https://doi.org/10.1107/s2059798317011597. https://www.ncbi.nlm.nih.gov/pubmed/28876235.

49. Rambo, R. P., and J. A. Tainer. 2011. Characterizing flexible and intrinsically unstructured biological macromolecules by SAS using the Porod-Debye law. *Biopolymers.* 95:559–571. https://doi.org/10.1002/bip.21638. https://www.ncbi.nlm.nih.gov/pubmed/21509745.

50. Orthaber, D., A. Bergmann, and O. Glatter. 2000. SAXS experiments on absolute scale with Kratky systems using water as a secondary standard. *J. Appl. Crystallogr.* 33:218–225. https://doi.org/10.1107/s0021889899015216.

51. Guinier, A., and G. Fournet. 1955. Small angle scattering of X-rays. Wiley, New York, p. 24.

52. Ibel, K., and H. Stuhrmann. 1975. Comparison of neutron and X-ray scattering of dilute myoglobin solutions. *J. Mol. Biol.* 93:255–265. https://doi.org/10.1016/0022-2836(75)90131-X.

53. Whitten, A. E., D. A. Jacques, …, D. B. Langley. 2007. The structure of the KinA-Sda complex suggests an allosteric mechanism of histidine kinase inhibition. *J. Mol. Biol.* 368:407–420. https://doi.org/10.1016/j.jmb.2007.01.064. https://www.ncbi.nlm.nih.gov/pubmed/17350039.

54. Olah, G. A., S. E. Rokop, …, J. Trewhella. 1994. Troponin I encompasses an extended troponin C in the Ca2+-bound complex: a small-angle X-ray and neutron scattering study. *Biochemistry.* 33:8233–8239. https://doi.org/10.1021/bi00193a009.

55. Moore, P. B. 1981. On the estimation of the radius of gyration of the subunits of macromolecular aggregates of biological origin in situ. *J. Appl. Crystallogr.* 14:237–240. https://doi.org/10.1107/s0021889881009278.

56. Moore, P. B., D. M. Engelman, and B. P. Schoenborn. 1974. Asymmetry in the 50S ribosomal subunit of Escherichia coli. *Proc. Natl. Acad. Sci. U S A.* 71:172–176. https://doi.org/10.1073/pnas.71.1.172.

57. Grant, T. D. 2018. Ab initio electron density determination directly from solution scattering data. *Nat. Methods.* 15:191–193. https://doi.org/10.1038/nmeth.4581.

58. Sumner, J., and S. Qian. 2022. DENSS-multiple: a structure reconstruction method using multiple contrast variation of small-angle neutron scattering based on the DENSS algorithm. Preprint at bioRxiv. https://doi.org/10.1101/2022.03.01.478978.

59. Petoukhov, M. V., and D. I. Svergun. 2005. Global rigid body modeling of macromolecular complexes against small-angle scattering data. *Biophys. J.* 89:1237–1250. https://doi.org/10.1529/biophysj.105.064154.

60. Berman, H. M., J. Westbrook, …, P. E. Bourne. 2000. The protein Data Bank. *Nucleic Acids Res.* 28:235–242. https://doi.org/10.1093/nar/28.1.235. https://www.ncbi.nlm.nih.gov/pubmed/10592235.

61. Goddard, T. D., C. C. Huang, …, T. E. Ferrin. 2018. UCSF ChimeraX: meeting modern challenges in visualization and analysis. *Protein Sci.* 27:14–25. https://doi.org/10.1002/pro.3235. https://www.ncbi.nlm.nih.gov/pubmed/28710774.

62. Kikhney, A. G., C. R. Borges, …, D. I. Svergun. 2020. SASBDB: towards an automatically curated and validated repository for biological scattering data. *Protein Sci.* 29:66–75. https://doi.org/10.1002/pro.3731. https://www.ncbi.nlm.nih.gov/pubmed/31576635.

63. Manalastas-Cantos, K., P. V. Konarev, N. R. Hajizadeh…, 2021. ATSAS 3.0: expanded functionality and new tools for small-angle scattering data analysis. *J. Appl. Cryst.* 54:343–355. https://doi.org/10.1107/S1600576720013412.

64. Brookes, E., and M. Rocco. 2018. Recent advances in the UltraScan SOlution MOdeller (US-SOMO) hydrodynamic and small-angle scattering data analysis and simulation suite. *Eur. Biophys. J.* 47:855–864. https://doi.org/10.1007/s00249-018-1296-0.

65. Putnam, C. D., M. Hammel, …, J. A. Tainer. 2007. X-ray solution scattering (SAXS) combined with crystallography and computation: defining accurate macromolecular structures, conformations and assemblies in solution. *Q. Rev. Biophys.* 40:191–285. https://doi.org/10.1017/S0033583507004635. https://www.ncbi.nlm.nih.gov/pubmed/18078545.

66. Mylonas, E., and D. I. Svergun. 2007. Accuracy of molecular mass determination of proteins in solution by small-angle X-ray scattering. *J. Appl. Crystallogr.* 40:245–249. . Suppl 1. https://doi.org/10.1107/s002188980700252x.

67. Smith, K. W., and M. E. Stroupe. 2012. Mutational analysis of sulfite reductase hemoprotein reveals the mechanism for coordinated electron and proton transfer. *Biochemistry.* 51:9857–9868. https://doi.org/10.1021/bi300947a. https://www.ncbi.nlm.nih.gov/pubmed/23153334.

68. Venceslau, S. S., Y. Stockdreher, …, I. Pereira. 2014. The "bacterial heterodisulfide" DsrC is a key protein in dissimilatory sulfur metabolism. *Biochim. Biophys. Acta.* 1837:1148–1164. https://doi.org/10.1016/j.bbabio.2014.03.007. https://www.ncbi.nlm.nih.gov/pubmed/24662917.

69. Unzai, S. 2018. Analytical ultracentrifugation in structural biology. *Biophysical Rev.* 10:229–233. https://doi.org/10.1007/s12551-017-0340-0.

Biophysical Journal, Volume *121*

Supplemental information

Neutron scattering maps the higher-order assembly of NADPH-dependent assimilatory sulfite reductase

Daniel T. Murray, Nidhi Walia, Kevin L. Weiss, Christopher B. Stanley, Peter S. Randolph, Gergely Nagy, and M. Elizabeth Stroupe

SUPPLEMENTAL FIGURES

Neutron scattering maps the higher-order assembly of NADPH-dependent assimilatory sulfite reductase

Daniel T. Murray, Nidhi Walia, Kevin L. Weiss, Peter S. Randolph, Christopher B. Stanley, Gergely Nagy, M. Elizabeth Stroupe

Table S1: Concentrations of protein samples during SANS measurements.

Protein	% D_2O	Concentration (mg/mL)	Oligomeric state	Domain/protein composition
SiR	100	2.9	Dodecamer ($\alpha_8\beta_4$)	SiRFP/SiRHP
D-SiR (DSiR0)	0	4.5	Dodecamer ($\alpha_8\beta_4$)	SiRFP/D-SiRHP
D-SiR (DSiR20)	20	4.1	Dodecamer ($\alpha_8\beta_4$)	SiRFP/D-SiRHP
D-SiR (DSiR41)	41	11.3	Dodecamer ($\alpha_8\beta_4$)	SiRFP*/D-SiRHP
D-SiR (DSiR86)	86	11.2	Dodecamer ($\alpha_8\beta_4$)	SiRFP/D-SiRHP*
D-SiR (DSiR100)	100	4.2	Dodecamer ($\alpha_8\beta_4$)	SiRFP/D-SiRHP
SiRFP-60/D-SiRHP	0	5.5	Dimer ($\alpha\beta$)	Fld-linker-FNR/D-SiRHP
SiRFP-60/D-SiRHP	41	3.0	Dimer ($\alpha\beta$)	Fld-linker-FNR*/D-SiRHP
SiRFP-60/D-SiRHP	86	3.0	Dimer ($\alpha\beta$)	Fld-linker-FNR/D-SiRHP*
SiRFP-60/D-SiRHP	100	4.7	Dimer ($\alpha\beta$)	Fld-linker-FNR/D-SiRHP
SiRFP	100	3.0	Octamer (α_8)	Octamerization-Fld-linker-FNR
SiRHP	100	5.0	Monomer (β)	SiRHP

* An asterisk indicates the contrast-matched component

Table S2: Sedimentation velocity AUC parameters for SiR samples.

Protein	D-SiRHP	SiRFP	D-SiR
Oligomeric state	Monomer (β)	Octamer (α_8)	Dodecamer ($\alpha_8\beta_4$)
Theoretical MW (kDa)	64	571	802
Experimental			
AUC MW (kDa)	72	613	838
$S_{20,w}$	4.8	14.1	17.5
f/f_0	1.14	1.93	1.90
2D-SA RMSD	0.0077	0.0067	0.0056
US-SOMO			
$S_{20,w}$	4.9	14.4	16.8
f/f_0	1.16	1.71	1.87
R_g (Å)	24.9	83.9	108.0

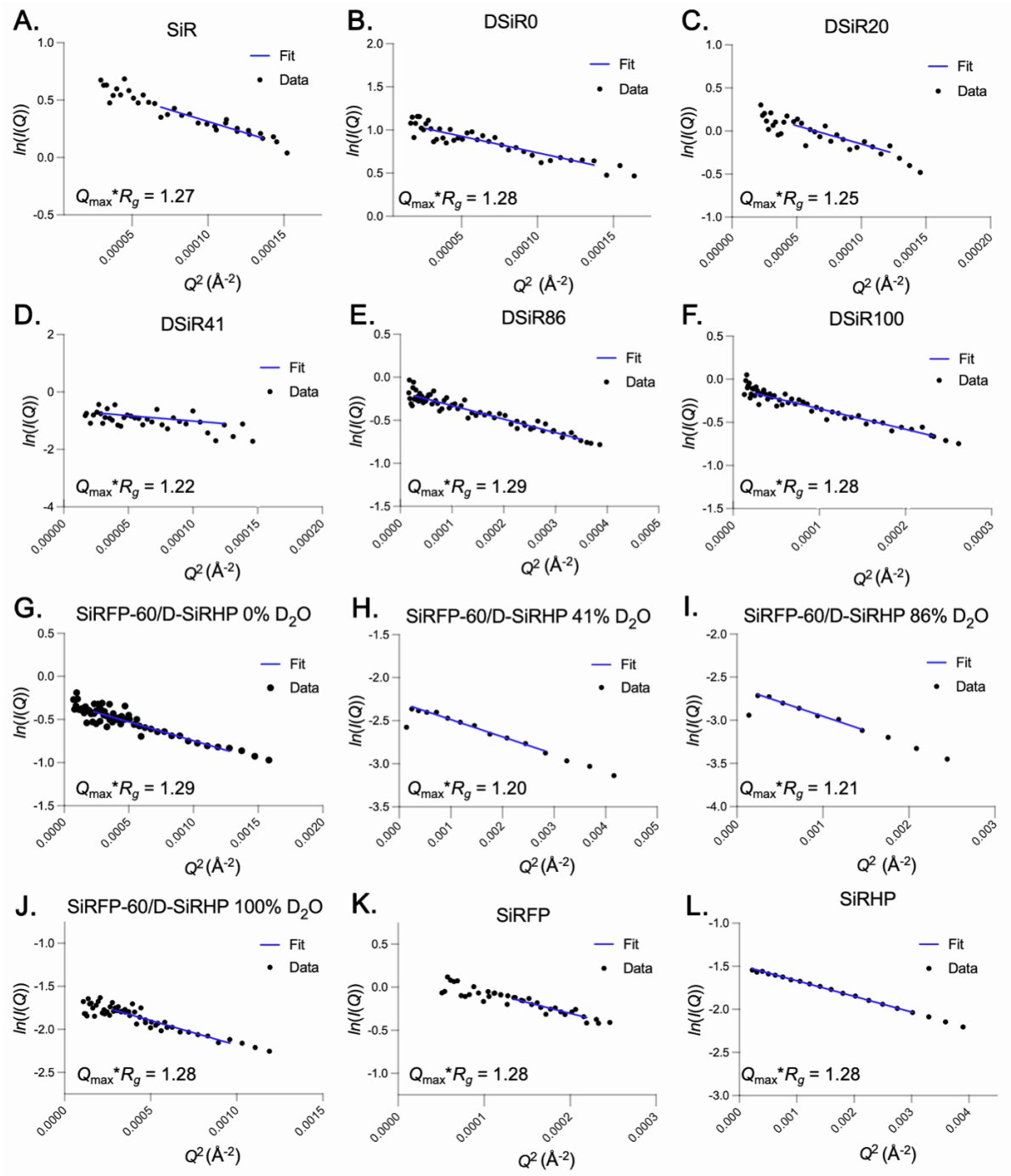

Figure S1: Guinier fits of the scattering data presented throughout the manuscript show each specimen to be monodisperse under all D_2O buffer conditions. $Q_{max} * R_g$ values are < 1.3 for all analyses.

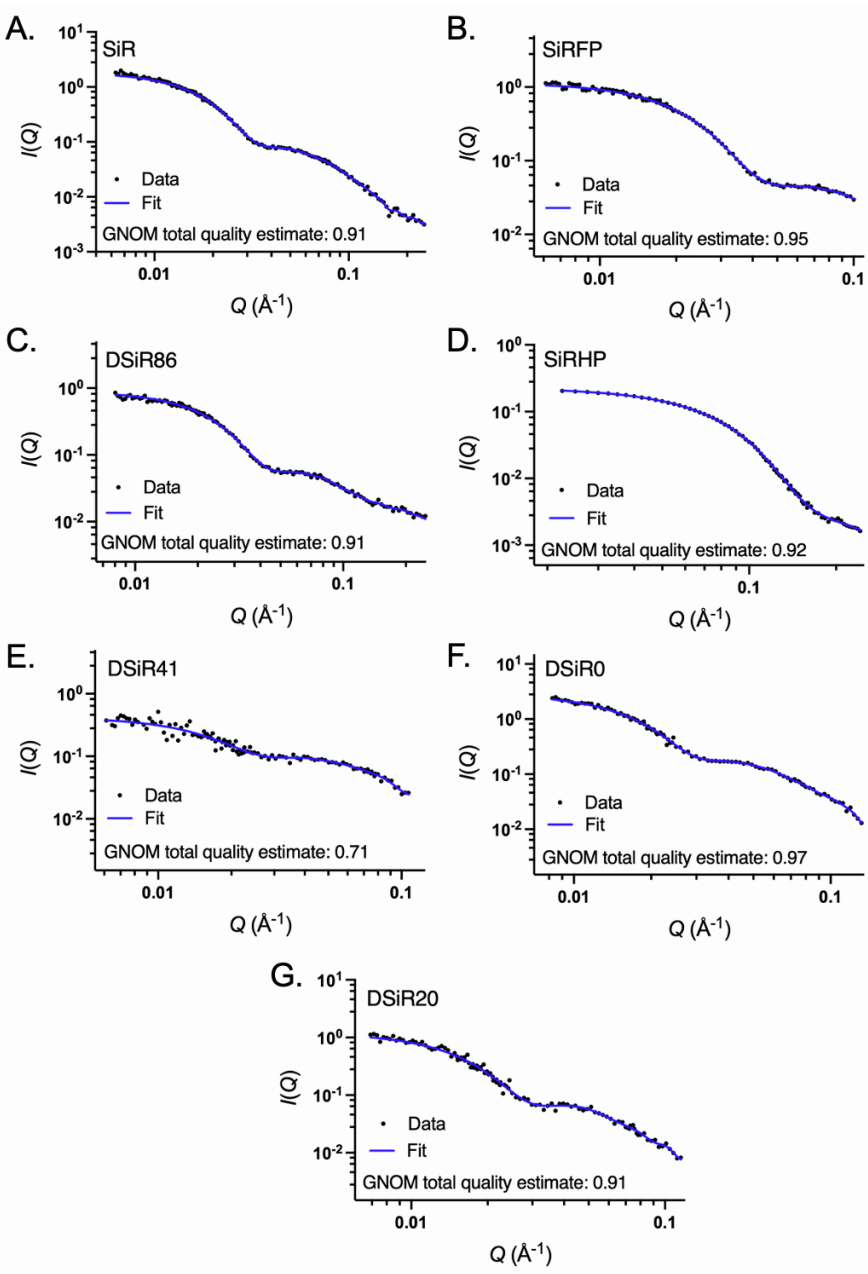

Figure S2: *P*(*r*) fits for the scattering data presented throughout the manuscript as calculated in GNOM, along with their quality-of-fit assessment as provided by the same software (1,2).

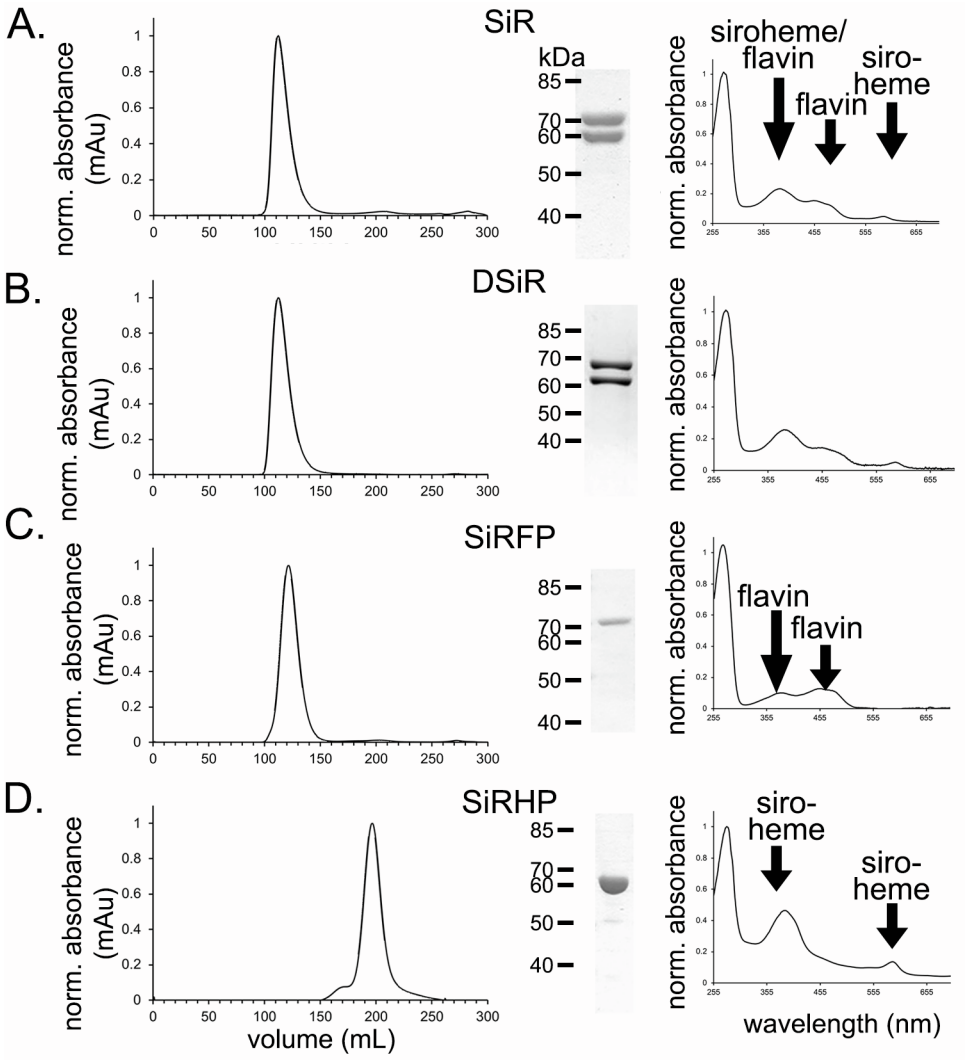

Figure S3: Reconstituted SiR resembles co-expressed SiR as seen by SEC, SDS-PAGE, and UV-Vis spectroscopy. Each SEC elution profile was obtained from a HiPrep 26/60 Sephacryl S-300 HR column (Cytiva, Marlborough, MA, USA). 12% SDS-PAGE gels were used for electrophoresis where the higher band (~70 kDa) represents SiRFP and the lower band (~60 kDa) represents SiRHP. UV-Vis spectra were obtained with an 8454 UV–Vis spectrophotometer (Agilent Technologies, Santa Clara, CA, USA). **A.** Co-expressed SiR; peak retention volume: 112 mL. **B.** Reconstituted D-SiR; peak retention volume: 112 mL. **C.** SiRFP; peak retention volume: 121 mL. **D.** SiRHP; peak retention volume: 197 mL.

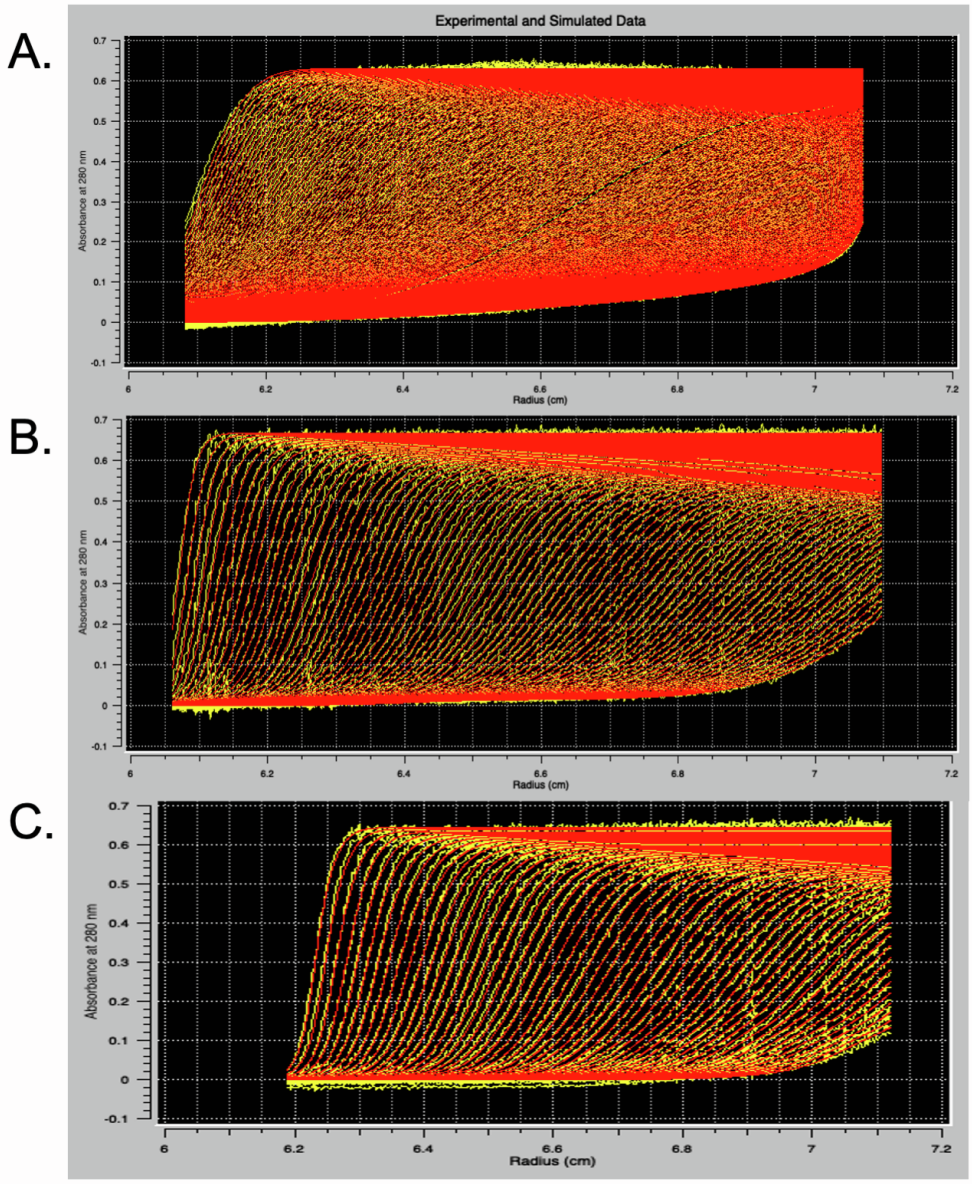

Figure S4: Sedimentation velocity scan data (yellow) with fits (red) from UltraScan III. **A.** D-SiRHP; **B.** SiRFP; **C.** D-SiR.

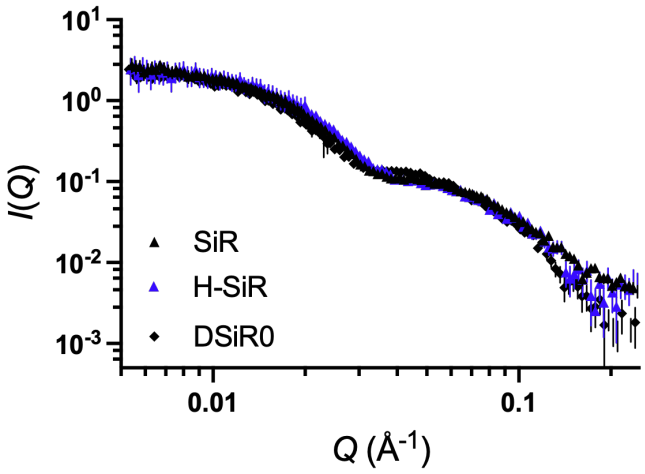

Figure S5: Reconstituted H-SiR and D-SiR scatter like their recombinantly-expressed counterpart, SiR. These experiments were performed at full contrast to measure the scattering of the entire complex, with SiR and H-SiR in 100% D_2O and D-SiR in 0% D_2O (DSiR0).

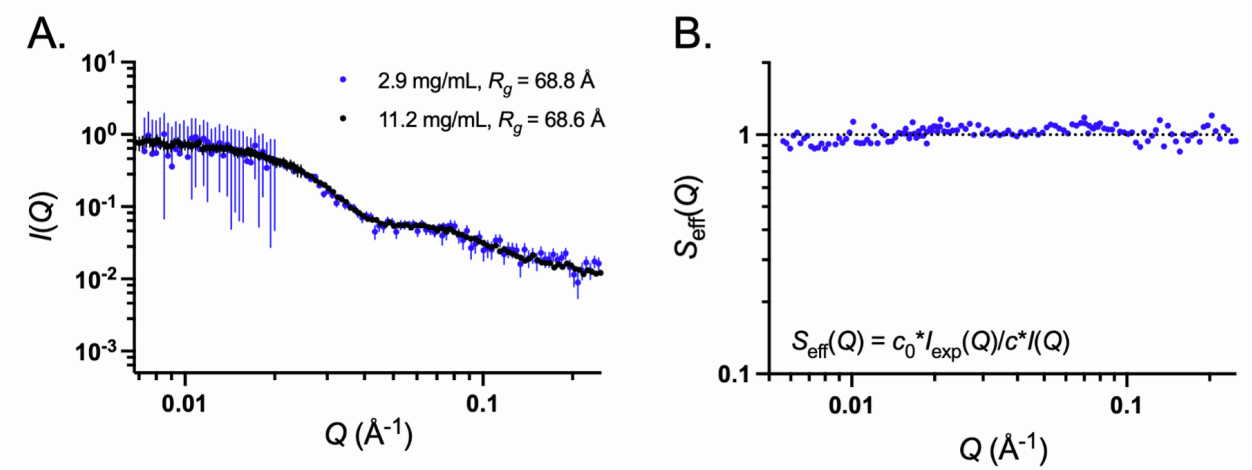

Figure S6: D-SiR is free from concentration and structure factor effects in the conditions used in this study. **A.** Scattering profiles of D-SiR at low and high concentrations yield similar R_g values. **B.** Effective structure factor analysis shows the absence of protein interactions during the experiment. The effective structure factor ($S_{eff}(Q)$) was obtained from the ratio of the experimental scattering intensity ($I_{exp}(Q)$) at a high concentration (c) to that measured ($I(Q)$) at a low concentration (c_0) where it is assumed interparticle interactions are negligible (1). If $S_{eff}(Q) < 1$, the net interactions are repulsive. If $S_{eff}(Q) > 1$, the net interactions are attractive. If $S_{eff}(Q) = 1$, the interparticle interactions are negligible.

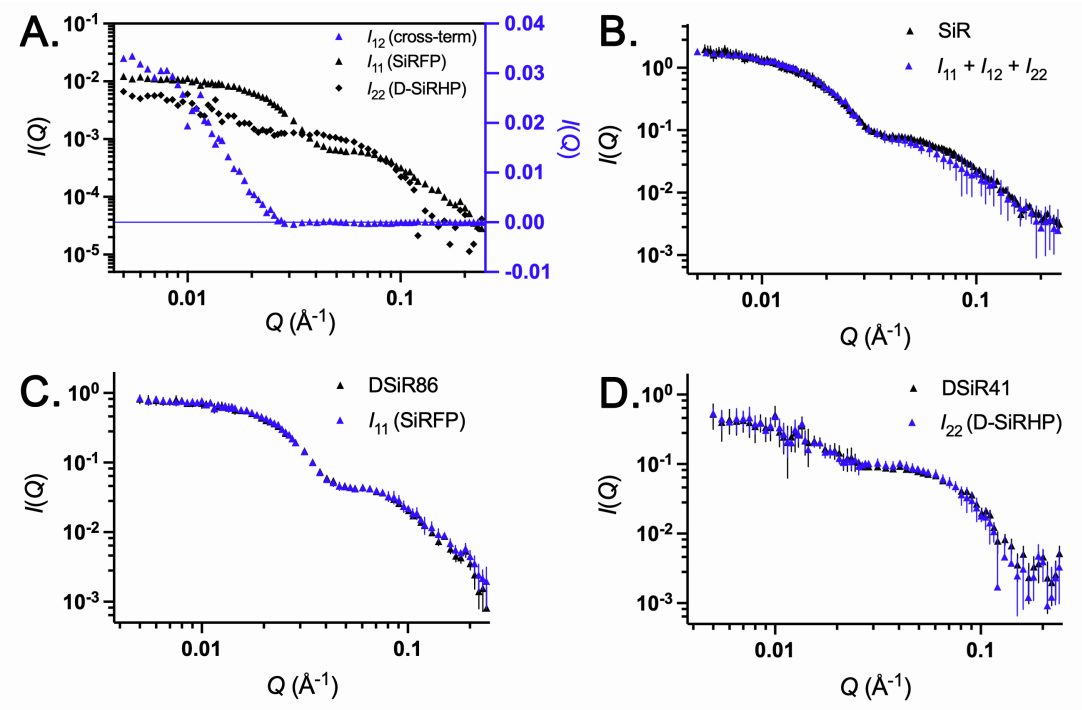

Figure S7: Composite scattering functions of the two-component D-SiR obtained from its NCV series. The scattering, $I(Q)$, of a two-component system with differing component contrasts can be approximated by (Equation S1):

$$I(Q) = \Delta\rho_1^2 I_1(Q) + \Delta\rho_1\Delta\rho_2 I_{12}(Q) + \Delta\rho_2^2 I_2(Q),$$

where $I_1(Q)$ and $I_2(Q)$ are the scattering intensities of components 1 and 2, respectively, and $I_{12}(Q)$ is the scattering intensity from interference between the two components because of their differing SLD (3). $I_1(Q)$ and $I_2(Q)$ describe the shapes of each component and $I_{12}(Q)$, or the "cross-term", describes the spatial distribution between them. Given a measured NCV series and calculated contrasts, $I_1(Q)$, $I_2(Q)$, and $I_{12}(Q)$ may be solved to obtain the composite scattering functions for a two-component system (4). This analysis may be used to aid modeling of protein subunit positions within a complex (3,5). The decomposition of an NCV series into approximated scattering functions for each component, along with the determination of a cross-term, were performed in the Compost module of MULCh (4). **A.** Decomposition of D-SiR's NCV series provides the composite scattering functions (log-log scale) and cross-term (semi-log scale) of the complex. **B.** SiR's scattering profile superimposed on the summed composite scattering functions. **C.** DSiR86's scattering profile superimposed on that of the composite scattering function of SiRFP within the reconstituted D-SiR dodecamer. **D.** DSiR41's scattering profile superimposed on that of D-SiRHP in the context of D-SiR.

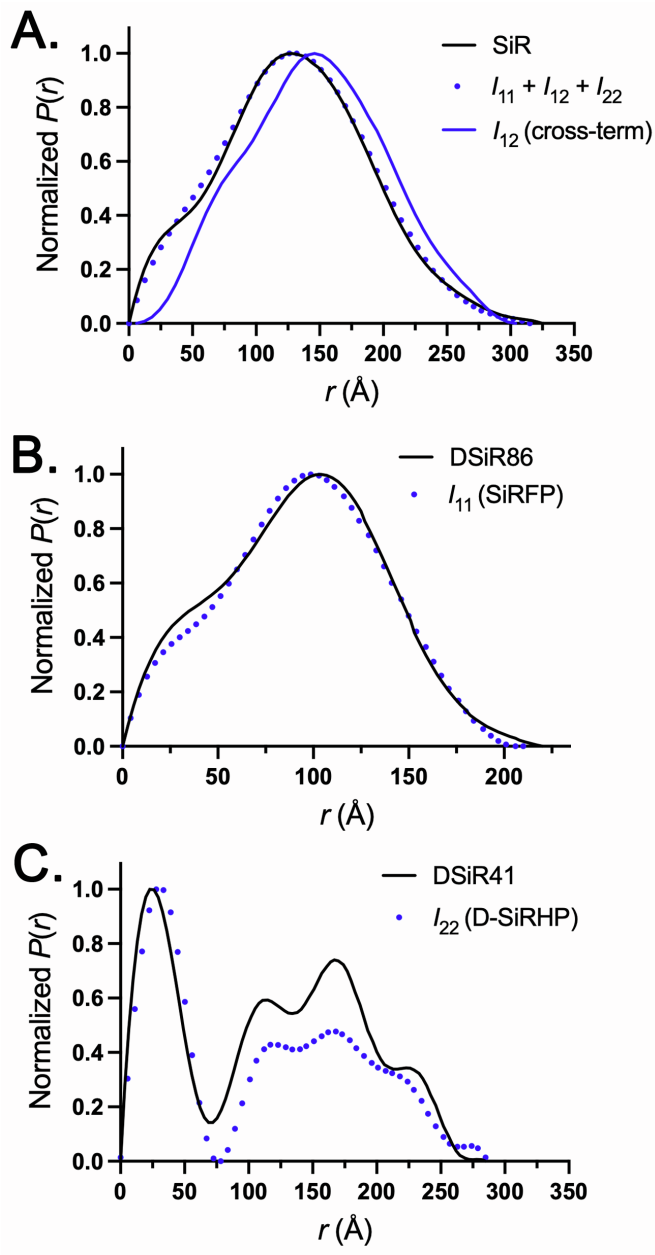

Figure S8: *P*(*r*) functions of the raw scattering data agree with that of the composite scattering functions. **A.** The *P*(*r*) plots of SiR, summed composite scattering functions, and cross-term. The cross-term's *P*(*r*) reveals the spatial distribution of SiRFP and D-SiRHP in complex. **B.** DSiR86 and composite scattering function of SiRFP. **C.** DSiR41 and composite scattering function of D-SiRHP.

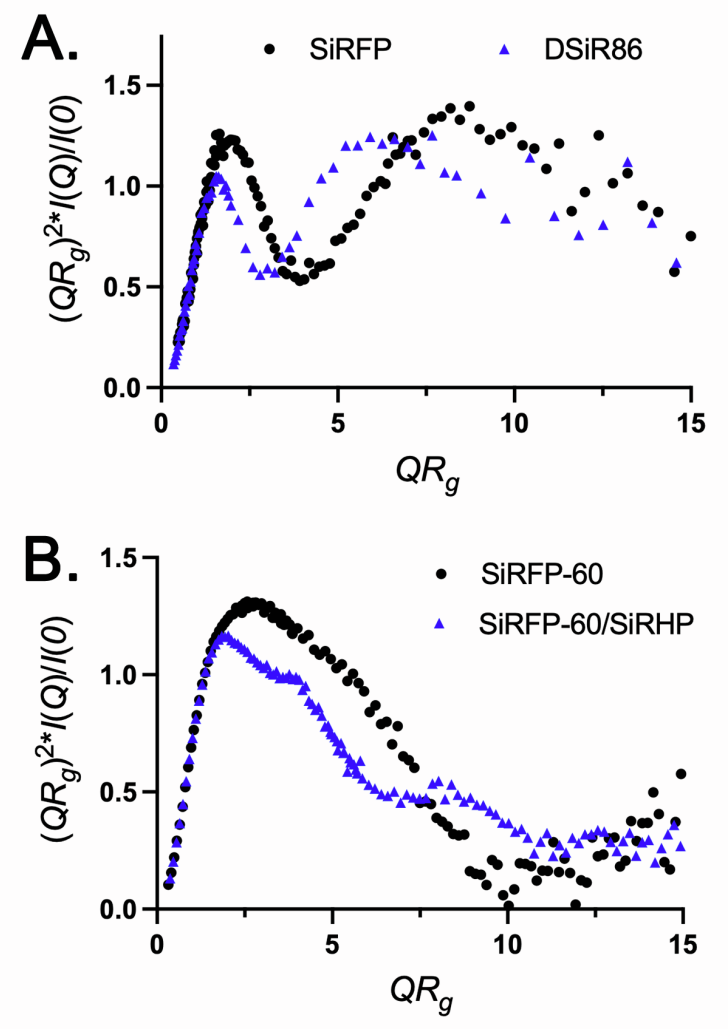

Figure S9: Dimensionless Kratky plots demonstrating the effect of intrinsically disordered regions in SiR proteins on their respective flexibilities. **A.** Complex formation does not diminish flexibility in SiRFP as exhibited by plateaus persisting into higher QR_g regions for both SiRFP and DSiR86. **B.** Flexibility due to the linker connecting the Fld and FNR domains in SiRFP-60 is present in its monomer as well as its heterodimer complex with SiRHP, whose plot contains features of a multi-lobed, globular particle with a flexible linker (6,7).

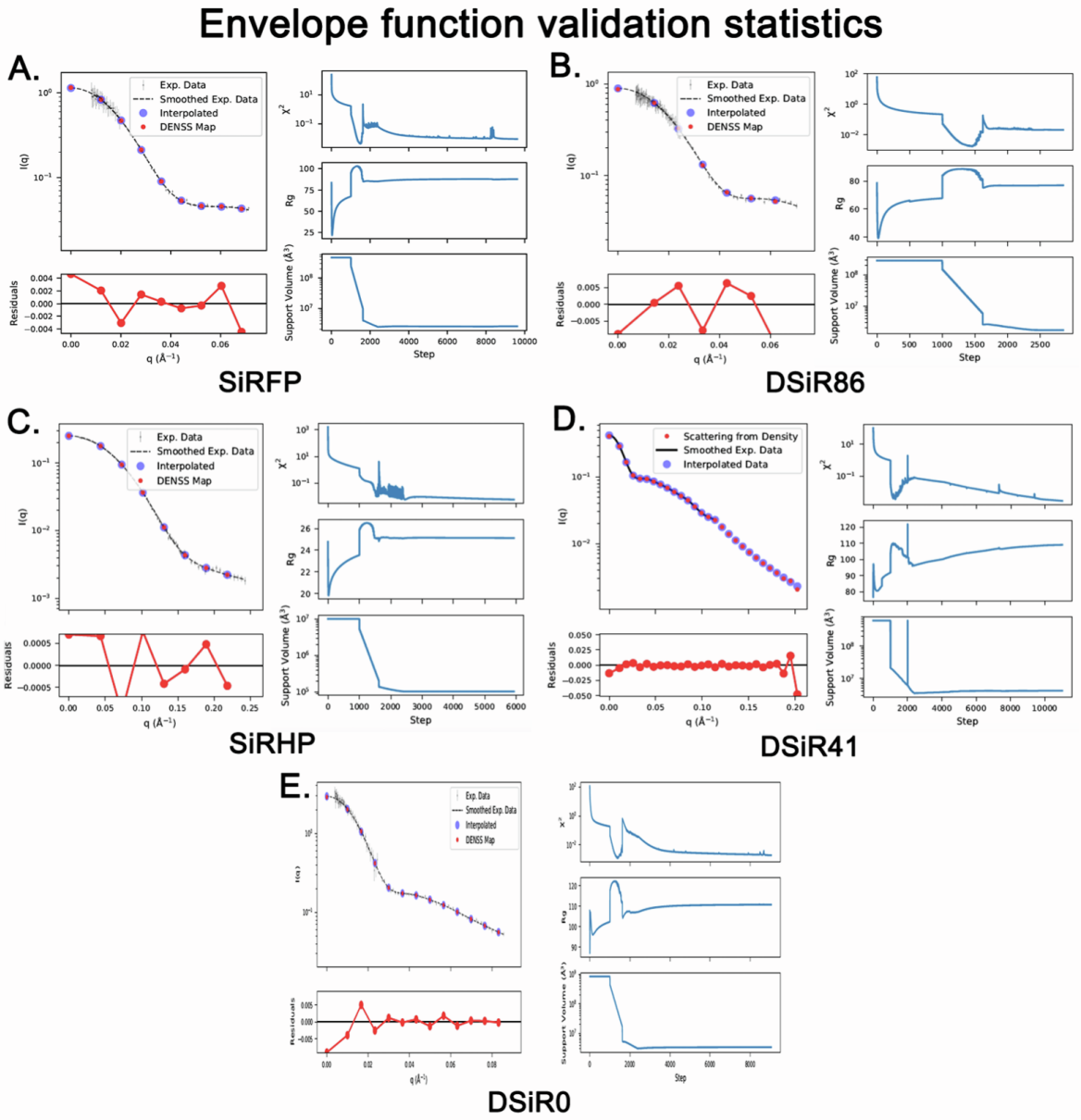

Figure S10: Theoretical scattering profiles calculated from *ab initio* models fit their experimental data (8). For each panel, the top left plot shows scattering from the modeled density fit to its experimental data and the bottom left plot shows the residuals of the fit. Plots to the right in each panel show χ^2 (top), R_g (middle), and support volume (bottom) converging through the course of modeling steps. **A.** SiRFP; **B.** DSiR86; **C.** SiRHP; **D.** DSiR41; **E.** DSiR0.

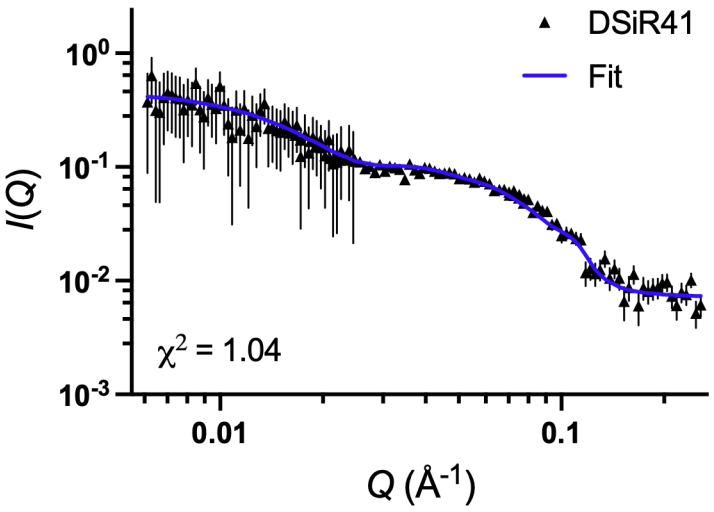

Figure S11: A fit between the theoretical scattering of four SiRHP subunits placed by rigid body modeling and DSiR41's experimental scattering shows suitable agreement.

References

1. Svergun, D. I. 1992. Determination of the regularization parameter in indirect-transform methods using perceptual criteria. *Journal of Applied Crystallography*. 25(4):495-503, doi: 10.1107/s0021889892001663, https://onlinelibrary.wiley.com/doi/abs/10.1107/S0021889892001663.
2. Trewhella, J., A. P. Duff, D. Durand, F. Gabel, J. M. Guss, W. A. Hendrickson, G. L. Hura, D. A. Jacques, N. M. Kirby, A. H. Kwan, J. Perez, L. Pollack, T. M. Ryan, A. Sali, D. Schneidman-Duhovny, T. Schwede, D. I. Svergun, M. Sugiyama, J. A. Tainer, P. Vachette, J. Westbrook, and A. E. Whitten. 2017. 2017 publication guidelines for structural modelling of small-angle scattering data from biomolecules in solution: an update. *Acta Crystallogr D Struct Biol*. 73(Pt 9):710-728, doi: 10.1107/S2059798317011597, https://www.ncbi.nlm.nih.gov/pubmed/28876235.
3. Zaccai, N. R., C. W. Sandlin, J. T. Hoopes, J. E. Curtis, P. J. Fleming, K. G. Fleming, and S. Krueger. 2016. Deuterium Labeling Together with Contrast Variation Small-Angle Neutron Scattering Suggests How Skp Captures and Releases Unfolded Outer Membrane Proteins. *Methods Enzymol*. 566:159-210, doi: 10.1016/bs.mie.2015.06.041, https://www.ncbi.nlm.nih.gov/pubmed/26791979.
4. A. E. Whitten, S. Cai, and J. Trewhella. 2008. M*ULCh*: modules for the analysis of small-angle neutron contrast variation data from biomolecular assemblies. *Journal of Applied Crystallography*. 41:222-226.
5. Whitten, A. E., D. A. Jacques, B. Hammouda, T. Hanley, G. F. King, J. M. Guss, J. Trewhella, and D. B. Langley. 2007. The structure of the KinA-Sda complex suggests an allosteric mechanism of histidine kinase inhibition. *J Mol Biol*. 368(2):407-420, doi: 10.1016/j.jmb.2007.01.064, https://www.ncbi.nlm.nih.gov/pubmed/17350039.
6. Murray, D., K. Weiss, C. Stanley, G. Nagy, and M. E. Stroupe. 2021. Small-angle neutron scattering solution structures of NADPH-dependent sulfite reductase. *Journal of Structural Biology*. 213(2):107724, doi: https://doi.org/10.1016/j.jsb.2021.107724.
7. Tavolieri, A. M., D. T. Murray, I. Askenasy, J. M. Pennington, L. McGarry, C. B. Stanley, and M. E. Stroupe. 2019. NADPH-dependent sulfite reductase flavoprotein adopts an extended conformation unique to this diflavin reductase. *J Struct Biol*. 205(2):170-179, doi: 10.1016/j.jsb.2019.01.001, https://www.ncbi.nlm.nih.gov/pubmed/30654136.
8. Grant, T. 2018. Ab initio electron density determination directly from solution scattering data. *Nature Methods*. 15:191-193.